Assessing Cloud Representation in Two Microphysics Schemes of MPAS-Atmosphere Model (version 8.2.2) over the Maritime Continent with Himawari-9 AHI Observations

Xuewei Zhang,[1,3*] Lipeng Jiang,[1,4] Zhiquan Liu[1*], Tao Sun[2], Wei Wang[1], I-Han Chen[2]

[1]NSF National Center for Atmospheric Research, Boulder, Colorado, USA
[2]Centre for Climate Research Singapore, Singapore
[3]Key Laboratory of Meteorological Disaster, Ministry of Education (KLME)/Joint International Research Laboratory of Climate and Environment Change (ILCEC)/Collaborative Innovation Center on Forecast and Evaluation of Meteorological Disasters (CIC-FEMD), Nanjing University of Information Science & Technology, Nanjing, China
[4]Earth System Modeling and Prediction Center, China Meteorological Administration, Beijing, China

Correspondence to: Xuewei Zhang (xwzhang@nuist.edu.cn) and Zhiquan Liu (liuz@ucar.edu)

Abstract. Tropical cloud prediction over the Maritime Continent remains challenging for numerical weather prediction models, largely due to uncertainties in cloud microphysics parameterizations under complex topography and multiscale convective conditions. Accurate cloud forecasts are essential for assimilating cloud-affected observations, particularly high-resolution radiances from geostationary satellites, which also provide a valuable basis for diagnosing model performance of clouds. In this study, tropical cloud characteristics simulated by the Model for Prediction Across Scales–Atmosphere (MPAS-A) with two cloud microphysics schemes—the single-moment WSM6 and the double-moment NSSL, are comprehensively evaluated using multi-band radiances from the Himawari-9 Advanced Himawari Imager (AHI) and associated Level-2 cloud products. The proposed infrared radiance–based framework enables more effective use of high-resolution satellite data for model assessment. Results indicate that NSSL better captures the spatial distribution of cloud amount and exhibits smaller warm forecast-minus-observation (F–O) brightness-temperature (BT) biases in cloud-sensitive window channels. In contrast, WSM6 shows smaller biases in water-vapor-sensitive channels but shows less skill in distinguishing cloudy and clear-sky conditions during the spin-up period. Cloud-type diagnostics further reveal opposite characteristics in the upper troposphere, with WSM6 underpredicting and NSSL overpredicting the occurrence of cold ice clouds. Nevertheless, both schemes show higher forecast skills for liquid-water and thin ice clouds than for other cloud types, whereas the largest forecast errors occur in multilayer ice-cloud regimes. An overprediction of cloud-top heights for high-level clouds is also evident in both schemes, with diurnal variations in F–O being more pronounced over land in NSSL.

1 Introduction

Cloud prediction in the tropics has long posed a major scientific and operational challenge due to the deep convection, complex multiscale interactions, sparse in situ observations, and strong ocean–atmosphere–radiation coupling that remain difficult for numerical models to represent (Jin et al., 2018; Medeiros et al., 2021; Gehne et al., 2022; Stephens et al., 2024). Within the tropical belt (~10° N–10° S, 90°–150° E), the Maritime Continent is characterized by exceptional complexity, with numerous islands, shallow seas, and rugged mountainous terrain that further complicate weather prediction (Neale and Slingo, 2003; Chang et al., 2016; Dipankar et al., 2020; Aslam, 2025). Despite the deployment of convection-permitting models with increasingly high spatial resolution, the accurate representation of cloud microphysical processes in this region remains unresolved, and forecast skill continues to be constrained by uncertainties in microphysics parameterizations under such complex boundary and atmospheric conditions (Khain et al., 2015; Chow et al., 2016; Simón-Moral et al., 2021; Lee et al., 2022).

In numerical weather prediction (NWP) systems, microphysical parameterizations play a fundamental role in regulating cloud simulations by governing hydrometeor classification, interactions between species, latent heat release, and radiative properties, all of which form a complex microphysical–dynamical–radiative coupling mechanism (Fovell et al., 2010; Zhang et al., 2021; Morrison et al., 2020; Köcher et al., 2023; Atlas et al., 2024). Commonly used schemes are broadly categorized into single-moment and double-moment approaches, whose different representations of hydrometeor mass and number concentration lead to distinct particle size distributions, sedimentation characteristics, and phase partitioning. Each cloud microphysics scheme relies on specific assumptions regarding cloud and precipitation hydrometeor properties, which can be a significant source of model error (Tong and Xue, 2008). Moreover, the effectiveness of assimilating cloud-affected satellite observations is strongly influenced by the representation of cloud microphysics (Sieron et al., 2017; Rendon et al., 2025). For example, inter-scheme differences in the treatment of latent cooling within the background state vector and associated error covariance matrices may affect data assimilation performance (Wheatley et al., 2014). Differences in hydrometeor fall velocities likewise alter background brightness temperatures (BTs) in data assimilation, as faster sedimentation transports hydrometeors from cloud tops to lower altitudes, resulting in higher simulated BTs (van Weverberg et al., 2013; Jones et al., 2018; Griffin and Otkin, 2022). In addition, simulated BTs are highly sensitive to the hydrometeor profiles provided to the radiative transfer model (Wang, Chipilski, et al., 2020; Wang, Su, et al., 2020; Li et al., 2022). Consequently, systematic assessment and refinement of cloud microphysics parameterization schemes remain a key prerequisite for improving model cloud predictability.

Given the sparsity of in situ observations and the limited spatial coverage of ground-based measurements in the tropics, satellite observations have become an indispensable basis for evaluating cloud parameterization schemes (Jones et al., 2013; Centurioni et al., 2019; Battaglia et al., 2020). Among these, microwave radiances provide valuable information on the vertical structure of hydrometeors (Matsui et al., 2014; Panegrossi et al., 2016; Galligani et al., 2017; Zhang et al., 2019). However, their relatively coarse temporal sampling, constrained by sun-synchronous orbits, limits their ability to continuously capture

the diurnal variability of clouds (Wang and Zhao, 2017). In contrast, geostationary infrared (IR) observations offer high-frequency, spatially continuous coverage over broad regions, enabling detailed monitoring of cloud systems and their diurnal evolution (Bessho et al., 2016; Schmit et al., 2017; Aumann et al., 2018; Susskind et al., 2019; Min et al., 2020).

Two general approaches are commonly used to assess cloud microphysics parameterization schemes with satellite observations. The first approach is based on direct comparisons between model-simulated hydrometeors and their satellite-retrieved counterparts (Waliser et al., 2009; Huang et al., 2019). This strategy typically relies on interpretable retrieval-based quantities, such as cloud fraction, cloud optical depth, and cloud-top height (CTH), derived from well-established retrieval algorithms (Otkin and Greenwald, 2008; Hashino et al., 2013; Wang et al., 2022; Mohan et al., 2024). These quantities either correspond directly to model prognostic variables or maintain strong physical relationships with them. For example, cloud-property products retrieved from visible and infrared satellite radiances have been widely used to diagnose systematic errors in the simulation of cloud fields (Franklin et al., 2013; Iwabuchi et al., 2016; Geiss et al., 2021; Guo et al., 2024). Using Geostationary Operational Environmental Satellite-9 (GOES-9) cloud-property products, Van Weverberg et al. (2013) further demonstrated that simulations of mesoscale convective systems over the tropical western Pacific are highly sensitive to microphysical parameterizations, particularly to the fall velocity of frozen condensate, which is closely related to particle size distributions.

The second approach employs a model-to-satellite framework, in which atmospheric fields from model output (e.g., temperature, water vapor, and cloud mixing ratios) are converted into simulated radiances or BTs via a forward radiative transfer model, enabling direct comparison with satellite observations (Cintineo et al., 2014; Zhang et al., 2019). This approach mitigates uncertainties associated with retrieval assumptions and provides a physically consistent linkage between model-simulated atmospheric states and satellite-observed radiances. As a result, the model-to-satellite strategy has been widely adopted for evaluating the realism of weather and climate model simulations (Otkin et al., 2009, 2017; Grasso et al., 2014; Yao et al., 2018). For instance, several studies have simulated geostationary imager infrared radiances to examine cloud coverage, diurnal variability, and cloud-property characteristics during high-impact convective events (Line et al., 2016; Griffin et al., 2017a, b; Lindsey et al., 2018). Using GOES channel-4 infrared observations, Thompson et al. (2016) highlighted that realistic representation of ice-cloud radiation properties requires explicit coupling between cloud microphysics and radiative parameterizations. The diurnal and semidiurnal variability of southeastern Pacific stratocumulus clouds was quantitatively evaluated by Painemal et al. (2013) using GOES-10 geostationary observations, revealing increases in cloud-top height and cloud fraction during the early morning followed by afternoon decreases, as well as more complex semidiurnal oscillations in coastal clouds compared to offshore clouds. Furthermore, pronounced diurnal variability in high-level clouds over tropical land was identified through a joint analysis of AIRS and IASI infrared observations, with cloud-type-dependent phase and amplitude signals indicative of strong convective coupling (Feofilov et al., 2019). Growing attention has also been directed toward assessing cloud microphysics schemes within this model-to-satellite evaluation framework. By mapping clear- and cloudy-sky model states into GOES-13 BT space, Jones et al. (2018) demonstrated that convective precipitation within the Warn-on-Forecast System (WoFS) was more realistically represented by the NSSL double-moment microphysics scheme,

although cirrus coverage was substantially overestimated, whereas the Thompson scheme produced more accurate cloud fields overall. Similarly, model-to-satellite analyses based on GOES-13 infrared (10.7 μm) BTs indicate that the WRF single-moment six-class (WSM6) scheme tends to underestimate upper-level ice clouds, with observed anvils suggesting excessive conversion of cloud water to graupel (Grasso et al., 2014). When evaluating simulations against GOES-16 all-sky infrared radiances, Kim et al. (2024) further found that differences in simulated BTs were primarily affected by ice and snow fall velocities, with the NSSL and Morrison schemes producing lower BTs due to slower fall speeds, while the faster-falling ice in the WDM6 scheme resulted in higher BT values. Collectively, these studies highlight the strong diagnostic value of satellite-based verification for improving the representation of cloud microphysical processes in numerical models.

As one of the most advanced geostationary infrared imagers, the Advanced Himawari Imager (AHI) aboard Himawari-8/9 provides high spatiotemporal resolution observations across visible, shortwave-infrared, and thermal-infrared bands, enabling the retrieval of key cloud properties such as optical thickness, cloud type, and cloud-top temperature (Letu et al., 2019). Cloud properties retrieved from Himawari-8 AHI have demonstrated strong consistency with observations from MODIS, CloudSat, CALIPSO, and radiosondes, thereby confirming the reliability of AHI data for cloud evaluation (Liu et al., 2020). Furthermore, cross-comparisons between Himawari-8 and Himawari-9 AHI infrared observations demonstrate high inter-sensor consistency, with root-mean-square errors (RMSEs) below 1.7 K, comparable scan-angle characteristics, and only minor differences relative to RTTOV simulations for channels 7, 9, and 16 (Zhu et al., 2023). Collectively, these studies highlight the strong potential of AHI observations for evaluating model cloud microphysics in tropical regions.

Despite the aforementioned advances, the evaluation and understanding of cloud predictability associated with microphysics parameterization schemes over the Maritime Continent remain relatively limited. Moreover, previous studies have largely focused on either single infrared channels or cloud-retrieved products, which has limited the scope of model evaluation using geostationary infrared satellite observations. In this study, multi-band infrared radiances from the Himawari-9 Advanced Himawari Imager (AHI), together with corresponding Level-2 cloud products, are used to evaluate the performance of two microphysics schemes implemented in the Model for Prediction Across Scales–Atmosphere (MPAS-A) (Skamarock et al., 2012, 2018) in representing tropical cloud systems from multiple perspectives, including BT simulations, cloud amount, cloud-top height, cloud type, and diurnal variability. This synergistic approach is expected to enhance the effective use of satellite observations and to provide a more comprehensive characterization of cloud properties for model evaluation. The primary objective of this study is to offer valuable insights into improving tropical cloud forecasts within a high-resolution regional modelling framework and to lay the groundwork for future assimilation of cloud-affected infrared radiances over this region. The remainder of this paper is organized as follows. Section 2 introduces the datasets, methodology, and model configurations. The results are presented and discussed in Section 3, and Section 4 summarizes the main findings and outlines directions for future prospects.

2 Data, Methodology and Model Settings

2.1 Regional MPAS-Atmosphere model

The Model for Prediction Across Scales–Atmosphere (MPAS-A) solves the fully compressible, nonhydrostatic equations of atmospheric motion formulated in a height-based, hybrid terrain-following vertical coordinate (Skamarock et al., 2012, 2018). The horizontal discretization is implemented on an unstructured centroidal Voronoi mesh with C-grid staggering, in which horizontal velocity components are defined on cell edges, while other prognostic variables are located at cell centers. This unstructured mesh framework supports both global and regional simulations with quasi-uniform or variable-resolution meshes, allowing local refinement in targeted regions. In this study, forecasts are conducted with the MPAS-A Version 8.2.2 to evaluate its performance in simulating clouds over the Maritime Continent with two microphysics schemes: WSM6 and NSSL. Under a comparable configuration, the Thompson scheme has been shown to yield systematically lower precipitation forecast skill than WSM6 and NSSL (Chen et al., 2026) and is therefore excluded from the present evaluation.

WSM6 is widely used among microphysics schemes because of its high computational efficiency (Hong and Lim, 2006; Comin et al., 2018). Several studies have shown that WSM6 outperforms some other single-moment schemes in simulations of high-impact weather events, including tropical cyclones and organized convection (Kanase et al., 2015; Park et al., 2019; Huang et al., 2019a, b, 2020; Huo, 2024). Nevertheless, Sunny Lim et al. (2020) reported that WSM6 tends to overestimate precipitation in shallow cloud systems due to excessive cloud-ice production associated with deposition processes. Although NSSL-MP includes six hydrometeor species, the hail category was deactivated in this study; thus, the five active species are the same as in WSM6—cloud water (Qc), rain (Qr), cloud ice (Qi), snow (Qs), and graupel (Qg). Unlike the single-moment WSM6 scheme, NSSL employs a double-moment formulation that additionally prognoses hydrometeor number concentrations, allowing a more flexible representation of particle size distributions and associated microphysical processes (Mansell et al., 2010). Previous studies have demonstrated that the NSSL scheme exhibits superior performance in simulating cloud-base height, ice water content, and heavy-precipitation events compared with some single- and double-moment schemes (Gevorgyan, 2018; Wang, 2022; Nam, 2024). Although multi-moment microphysics schemes generally outperform single-moment schemes in representing size-sorting sedimentation and complex microphysical processes (Dawson et al., 2010; Milbrandt and McTaggart-Cowan, 2010; Wang et al., 2022), these advantages are not consistently realized. Several studies have reported only limited improvements relative to single-moment schemes (Van Weverberg et al., 2013, 2014; Igel et al., 2015; Cho et al., 2020; Li et al., 2020; Luo et al., 2024).

In light of these differences, comparative forecast experiments are conducted to assess the performance of two representative bulk microphysics schemes, namely WSM6 and NSSL, in simulating tropical cloud systems within the MPAS framework. Although both schemes predict the same set of hydrometeor species, their underlying parameterizations differ substantially (Hong and Lim, 2006; Mansell et al., 2010). In the NSSL scheme, particle size distributions are formulated using gamma functions of particle diameter or volume, whereas WSM6 assumes exponential size distributions with prescribed intercept parameters. Heterogeneous ice nucleation in WSM6 is parameterized as a temperature-dependent process, with ice

crystal number concentration diagnosed as a function of the ice mass field (Hong et al., 2004). In contrast, the NSSL scheme adopts the parameterizations of Ferrier (1994) and Meyers et al. (1992) for the initiation of pristine ice crystals.

The configuration of other physical parameterization schemes is summarized in Table 1. Cloud fraction is diagnosed using the Xu–Randall scheme, in which subgrid-scale cloudiness is parameterized as a function of grid-mean cloud water mixing ratio and relative humidity (Xu and Randall, 1996). The model domain, centered over Singapore (1.21° N, 102.0° E), covers a radius of approximately 1,120 km with a quasi-uniform horizontal resolution of 3 km, comprising 522,172 grid cells (Figure 1). The vertical grid consists of 65 model levels extending from the surface to 40 km. Twelve 48-h cold-start forecasts, initialized at 00:00 and 12:00 UTC, are conducted during two convective episodes from 26 to 28 September and from 3 to 5 October 2024 (Chen et al., 2026). ECMWF HRES analyses and the corresponding forecasts are interpolated onto the MPAS mesh to generate the initial and lateral boundary conditions for each cold-start forecast.

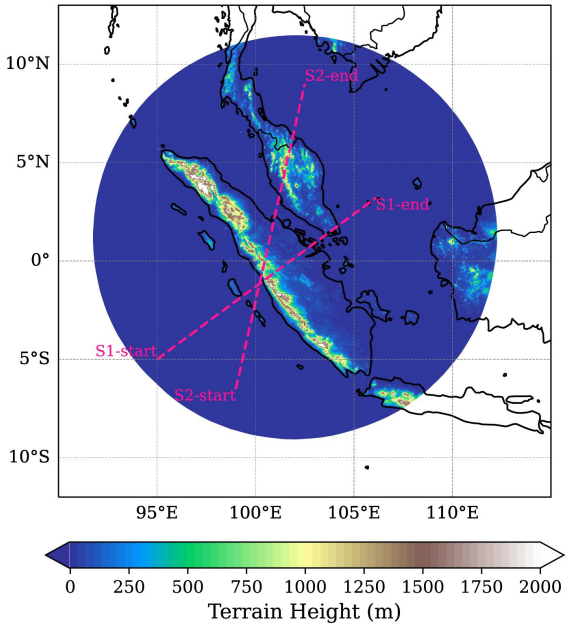


Figure 1. The terrain height (units: m) of MPAS simulation domain over the Maritime Continent, with three transects (S1–S2) used for subsequent cross-sectional analyses.

Table 1. MPAS Physics Configuration

Physics process	configuration
Boundary layer	MYNN
Surface layer	MYNN

Microphysics	WSM6 / NSSL
Convection	Grell-Freitas
Land surface	Noah
Shortwave/longwave Radiation	RRTMG
Cloud fraction for radiation	Xu-Randall
Gravity wave drag	YSU

2.2 Himawari-9 AHI Radiances and Retrieval Products

The Himawari-9 geostationary meteorological satellite, operated by the Japan Meteorological Agency (JMA), was launched on 2 November 2016 and became operational on 13 December 2022, when it succeeded Himawari-8. Its onboard Advanced Himawari Imager (AHI) provides full-disk observations every 10 min and regional imagery at temporal resolutions ranging from 2.5 min to 30 s, with spatial resolutions of 0.5 km in the visible bands and 2 km in the infrared bands. These high-frequency, high-resolution observations enable detailed analyses of cloud evolution and model performance.

Table 2 summarizes the key characteristics of AHI infrared channels 7–16, spanning wavelengths from 3.9 to 13.3 μm. AHI channel 7 (3.9 μm), located in the shortwave IR window, is sensitive to cloud phase and particle size variations and is widely used for nighttime cloud and fog detection, as well as low-level cloud identification. The water-vapor absorption bands (channels 8–10; 6.2, 6.9, and 7.3 μm) are primarily sensitive to mid- to upper-tropospheric humidity and cloud-top properties under cloudy conditions. The atmospheric-window bands 13–15 (10.4, 11.2, and 12.4 μm) are commonly applied in operational analyses for cloud-phase discrimination, low-level moisture monitoring, volcanic ash detection, and sea surface temperature retrieval, thereby supporting real-time NWP applications (Wang et al., 2018). In addition to channel 11 (8.6 μm), which is sensitive to cloud phase, the brightness temperature difference (BTD) between 8.6 μm and 11.2 μm (channel 14) serves as a key discriminator for cloud-type classification, with positive values typically associated with ice clouds and negative values indicating clear-sky or altocumulus conditions (Nasiri et al., 2008). Channel 16 (13.3 μm), located within the CO_2 absorption band, is used to infer cloud-top height and the optical thickness of thin cirrus clouds (Bessho et al., 2016). In this study, cloud microphysical properties are evaluated through simulations of AHI infrared radiances from channels 7–16, excluding the ozone-sensitive channel 12 (9.6 μm), which lies beyond the scope of this analysis.

In addition to Level-1 radiance data, fundamental cloud products from Himawari-9, comprising cloud mask, cloud type, and cloud-top information, are also used for evaluation at the same high resolution. These products are generated using retrieval

algorithms originally developed under the National Oceanic and Atmospheric Administration (NOAA) / National Environmental Satellite, Data, and Information Service (NESDIS) Enterprise project for the Geostationary Operational Environmental Satellite–R (GOES-R) Advanced Baseline Imager (ABI) (Imai et al., 2016). The binary cloud mask product is derived using the NOAA/NESDIS Enterprise Cloud Mask (ECM) methodology (Heidinger et al., 2018). Cloud-top-height is retrieved using the 13.3-μm CO_2 absorption band in combination with several longwave infrared window channels (10.4, 11.2, and 12.4 μm) (Heidinger et al., 2011, 2020). The cloud-type product is derived from four AHI infrared channels (7.3, 8.6, 11.2, and 12.4 μm) and classifies clouds into nine categories: fog, warm liquid water (WL), supercooled liquid water (SLW), mixed phase (MIXED), opaque ice (ICE), cirrus (semithin ice), overlap (with a semi-transparent upper layer), overshooting, and uncertain (UN) (Pavolonis et al., 2010; Pavolonis and Corey, 2020).

Table 2. Characteristics of Himawari-9 AHI infrared channels

Channel	Central wavelength (μm)	Spatial resolution (km)	Physical Properties
7	3.9	2	Low Cloud, Fog, Forest Fire
8	6.2	2	Mid- and Upper- Level Moisture
9	6.9	2	Mid-Level Moisture
10	7.3	2	Mid- and Lower- Level Moisture
11	8.6	2	Cloud Phase, Volcanic SO_2
12	9.6	2	Ozone
13	10.4	2	Clouds, Cloud Top Information
14	11.2	2	Clouds, Sea Surface Temperature
15	12.4	2	Clouds, Sea Surface Temperature
16	13.3	2	Cloud top height, CO2

2.3 Radiance Simulation with MPAS-JEDI and CRTM

This study uses the MPAS-JEDI system to perform all-sky radiance simulations over the model domain (Figure 1) and to compare the simulations with Himawari-9 AHI radiance observations. MPAS-JEDI (Liu et al., 2022; Guerrette et al., 2023; Jung et al., 2024; Sun et al., 2025) is a new-generation data assimilation system for MPAS-A, developed within the Joint Effort for Data assimilation Integration (JEDI) framework (Trémolet and Auligné, 2020). While MPAS-JEDI supports the assimilation of microwave and infrared radiance observations through the Community Radiative Transfer Model (CRTM) as the radiance observation operator (Liu and Weng, 2006; Chen et al., 2008; Johnson et al., 2023), this study applies the so-called *HofX* capability to forward-simulate AHI BTs from MPAS forecast outputs and to directly compare them with observations. To facilitate model–observation comparisons, hourly full-disk AHI radiance data and cloud products are remapped onto the regional MPAS unstructured mesh and converted into the Interface for Observation Data Access (IODA) format, which can be directly ingested by the MPAS-JEDI *HofX* application. In this study, CRTM version 2.4.1 is employed to simulate AHI radiances under all-weather conditions using geophysical inputs from MPAS forecasts, including profiles of pressure, temperature, water vapor, and the mixing ratios and effective radii of five hydrometeor species: cloud liquid water, cloud ice, rain, snow, and graupel. In the current MPAS-JEDI interface, the effective radii of cloud water, cloud ice, and snow used in CRTM are consistent with those diagnosed by the WSM6 and NSSL microphysics schemes. For rain and graupel, the effective radii used in CRTM are diagnosed following the particle-size-distribution assumptions of WSM6, whereas the corresponding NSSL-specific diagnostics have not yet been implemented. Specifically, constant effective radii are prescribed for rain and graupel in the CRTM calculations for the NSSL simulation, rather than values that vary with the particle size distributions represented by the NSSL microphysics. Surface emissivity is handled by the CRTM surface module, which accounts for four major surface types, including water, land, ice, and snow (Johnson et al., 2023).

3 Evaluation of Cloud Forecast

Based on AHI radiances and retrieval products, cloud representations in the WSM6 and NSSL microphysics schemes are examined from multiple perspectives, including cloudy-sky radiance simulations, cloud properties, and their diurnal evolution. A two-dimensional horizontal comparison is conducted between model-simulated and observed cloud states for each mesh cell. Model grid cells are classified as cloudy following the ECMWF diagnostic criterion, whereby the cloud fraction exceeds 1% and the total condensate of cloud liquid and ice is greater than 1×10^{-6} kg kg^{-1} (Serra et al., 2023). The observed cloudiness is determined using the AHI cloud mask, in which a value of 1 denotes cloudy conditions and 0 represents clear sky. The comparison results are presented in the following subsections.

3.1 Cloudy-Sky Radiance Simulation

Figure 2 presents the BT probability distributions of nine AHI infrared channels for the observations and for simulations using the two microphysics schemes. The statistics are derived from cloud-matched samples jointly identified by the observations

and each microphysics scheme. Given the comparable numbers of matched cloudy samples, with 17,184,742 matched samples for OBS-WSM6 and 17,238,036 for OBS-NSSL, the observational distributions show negligible differences between the two matching procedures, as shown in Figures 2a and 2c shown. For brevity, the observational results presented in the following sections are shown only for samples matched with the WSM6 simulations.

The observed AHI BTs exhibit pronounced inter-channel variability (Figures 2a and 2c), consistent with their spectral sensitivities summarized in Table 1. The water-vapor bands 8–10 show relatively narrow BT ranges with broad, high-frequency peaks between ~210–260 K, reflecting the prevalence of moisture in the middle to upper troposphere. Besides, the IR window channels 11 and 14–16 display a substantially broader BT range (~210–290 K) with similar frequency structures. The warm-side distribution of channel 13 (10.4 μm), a relatively "cleaner" IR window band, is shifted toward cooler BTs (~220–270 K) owing to reduced water-vapor attenuation and increased sensitivity to high cloud-top emission (Lindsey et al., 2012). Meanwhile, channel 7 (3.9 μm), which is strongly sensitive to low-level clouds and surface emission, yields the warmest and most right-skewed BT distribution among the AHI infrared channels.

Relative to the observations, both WSM6 and NSSL simulations reproduce the overall inter-channel hierarchy, yet exhibit notable differences in distribution width, frequency structure, and cold-tail characteristics. Verification against nighttime channel 7 (3.9 μm) observations shows that NSSL more closely reproduces the observed cold-end BT distribution below 250 K. For the water-vapor channels (8–10), WSM6 more closely matches the observed BT distributions, whereas NSSL exhibits larger departures, characterized by an expanded distribution toward colder BTs and a weakened warm-side peak. For the window channels (11 and 14–16), the observed BT range of 210–290 K is more realistically captured by NSSL, although it exhibits an extended cold tail around 200–210 K. This pronounced cold tail in the NSSL simulations indicates an overabundance of high-level clouds. Comparatively, WSM6 better reproduces the overall frequency structure, but its underestimation of cold BTs suggests insufficient high or optically thick cloud representation. Unlike the observed channel-13 BTs, which exhibits a distinctly narrower BT range and higher frequencies between 230 and 250 K, both WSM6 and NSSL produce broader distributions, indicating greater variability in the simulated cloud-top and upper-level ice-cloud properties. Moreover, both microphysics schemes exhibit a higher frequency of warm BTs around 280-295 K than observed. These warm BTs may be associated with semitransparent high-level clouds, consistent in some regions with the lower cloud ice water path (CIWP) and higher outgoing longwave radiation (OLR) shown in Figure 3. For such clouds, thermal emission from warmer underlying cloud layers and/or the surface can partially transmit through the cloud and contribute to the top-of-atmosphere radiance (Marchand et al., 2010; Wang et al., 2013). In addition, uncertainties in the AHI Level-2 cloud detection may also affect the warm-BT distribution. A similar contrast is evident across several cloud-sensitive infrared channels, with WSM6 exhibiting a greater occurrence of relatively warm BTs and NSSL extending more prominently toward lower BTs. This contrast suggests that NSSL tends to produce more high-level, cold clouds, whereas the warmer BT distribution in WSM6 may reflect a greater contribution from lower, warmer clouds.

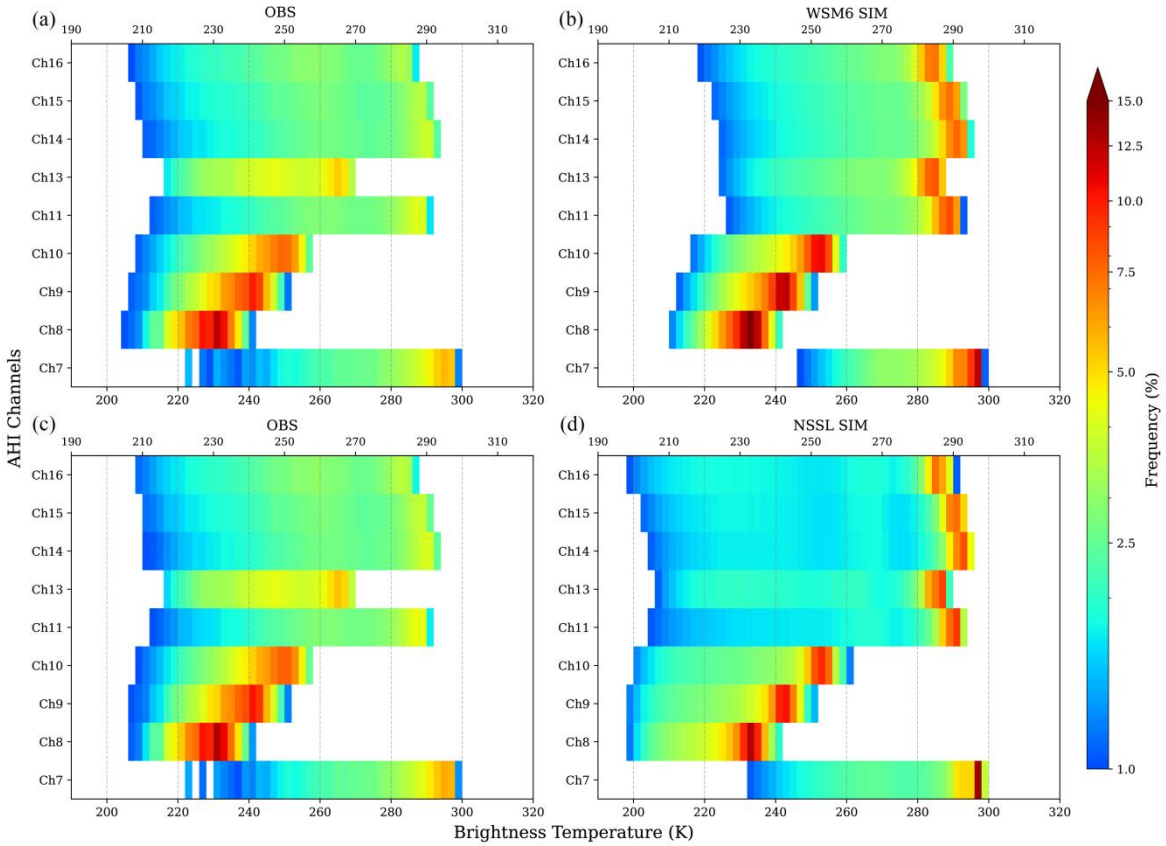


Figure 2. Frequency distributions (>1.0%) of AHI brightness temperatures (BTs; K) for channels 7–11 and 13–16 from (a, c) observations cloud-matched with WSM6 and NSSL, respectively, and the corresponding (b) WSM6 and (d) NSSL simulations. Statistics are computed from 24-48 h forecasts at 6 h intervals, except for channel 7 using only nighttime samples (12-18 h and 36-42h; 20:00-02:00 SGT).

To further interpret the AHI-based diagnostics from a physical-space perspective, Figure 3 presents the time-averaged horizontal distributions of forecast-minus-observation (F–O) BT differences for AHI channel 13, together with OLR and CIWP simulated by WSM6 and NSSL.

Both simulations exhibit predominantly positive F–O differences over the equatorial region and near parts of the domain boundary, consistent with the more frequent occurrence of relatively warm channel-13 BTs (>270 K) compared with the observations in Figure 2. WSM6 shows more widespread positive F–O departures, which generally coincide with higher OLR and lower CIWP, suggesting a reduced amount of upper-level ice clouds. In contrast, NSSL exhibits generally smaller F–O biases, particularly over the 5–10°N region, although negative departures remain in some areas. Regions with reduced warm F–O biases in NSSL generally correspond to lower OLR and substantially larger CIWP. This spatial relationship is also consistent with the channel-13 BT frequency distributions in Figure 2, where NSSL exhibits a greater occurrence of cold BTs below approximately 230 K, suggesting a greater occurrence of cold upper-level ice clouds. A larger ice water path generally increases cloud optical thickness, shifting the effective emission level toward colder upper-cloud layers and thereby resulting

in lower infrared window-channel brightness temperatures and reduced OLR (Marquis et al., 2023; Spang et al., 2024). The domain-averaged vertical hydrometeor profiles in Figure 8 provide further physical support by showing corresponding differences in upper-level frozen hydrometeor content between the two schemes.

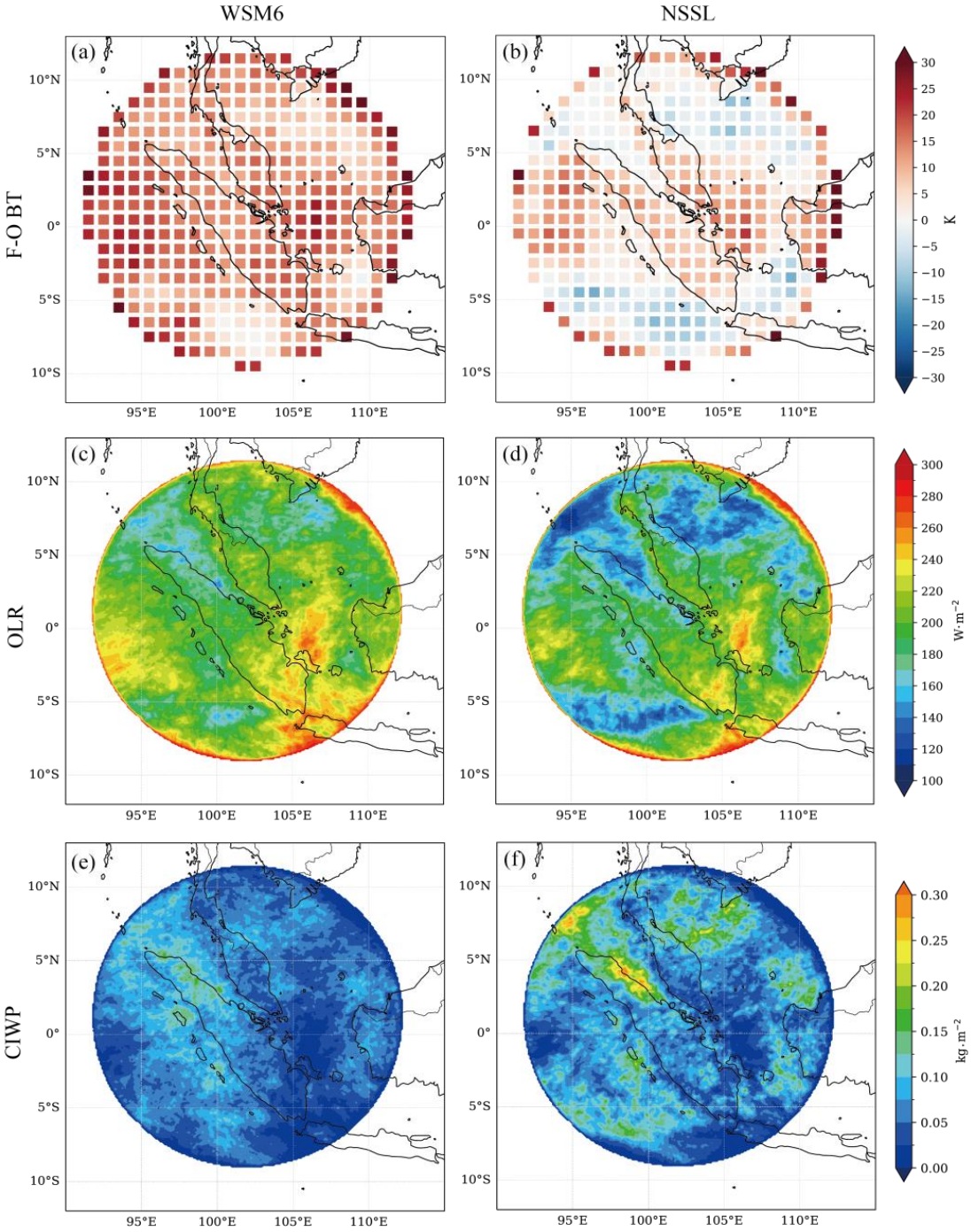


Figure 3. Daily-mean horizontal distributions of (a, b) AHI channel-13 forecast-minus-observation (F–O) brightness-temperature differences, (c, d) simulated outgoing longwave radiation (OLR), and (e, f) simulated cloud ice water path (CIWP) for WSM6 (left column) and NSSL (right column). Statistics are computed from 24-48 h forecasts at 6 h intervals using cloudy samples.

3.2 Cloud Amount, Cloud Type and Cloud-Top-Height

To evaluate the model performance in representing cloudiness, two metrics are used to quantify cloud-amount forecast skills: the Critical Success Index (CSI) and Negative Probability of Detection (PODN), which are formulated as follows (Grecu and Krajewski, 2000),

$$\mathrm{CSI} = \frac{\mathrm{Na}}{\mathrm{Na} + \mathrm{Nb} + \mathrm{Nc}}, \tag{1}$$

$$\mathrm{PODN} = \frac{\mathrm{Nd}}{\mathrm{Nb} + \mathrm{Nd}}. \tag{2}$$

Here, Na denotes the number of grid cells identified as cloudy by both MODEL and OBS (hits), Nb represents the number of grid cells classified as cloudy by MODEL but clear by OBS (false alarms), Nc refers to the number of grids identified as clear by MODEL but cloudy by OBS (misses), and Nd indicates the number of grids recognized as clear by both OBS and MODEL (correct negatives). These contingency relationships between observed and model cloudiness states are summarized in Table 3. For each metric, values approaching 1.0 indicate higher cloud forecast skill and closer agreement between the model and observations.

Figures 4c-d present CSI and PODN for the cloudiness forecast as a function of forecast lead time (Singapore local time) for WSM6 and NSSL. Besides, Figures 4a-b present the numbers of cloudy and clear-sky pixels identified separately by the observations and by the model with each microphysics scheme. It is noted that both schemes tend to overpredict cloudy pixels and underpredict clear-sky pixels relative to the observations. This common high cloud-top bias suggests potential deficiencies in the model's representation of cloud vertical development. These mismatched samples primarily correspond to "Oclear-Mcloud" situations, indicating inconsistencies between the model-simulated and observed cloudiness states.

As shown in Figures 4a-b, the observations indicate that cloud amount reaches its maxima during forecast hours 9–18 and 33–42 (17:00–02:00 SGT) and decreases to minima during forecast hours 21–27 and 45–48 (05:00–11:00 SGT). Both WSM6 and NSSL reproduce the overall temporal evolution, although the model simulated cloud maxima occurs relatively later than observed when the observed cloud amount peaks around 9 h and 33 h (Figure 4a). Consistently, the CSI for both schemes increases markedly during 9–21 h and 30–45 h (17:00–05:00 SGT), with pronounced declines around 21–27 h and 45–48 h (05:00–11:00 SGT; Figure 4c). These fluctuations closely coincide with the diurnal variation in cloudy-pixel counts shown in Figure 4a. In other words, cloud representation skill is higher during periods of cloud development and lower during cloud dissipation. Moreover, during the first 9 h, NSSL produces fewer cloudy pixels and more clear-sky pixels, in closer agreement with the observations, suggesting a more realistic spin-up of initial cloud development (Figure 4a). In contrast, WSM6 tends to overpredict cloud occurrence, with a subset of observed clear-sky pixels being erroneously classified as cloudy.

Correspondingly, higher CSI and PODN scores are achieved by NSSL within the first 9 h (Figures 4c-d). At later forecast times beyond 24 h, both schemes maintain relatively high CSI values (>0.7, Figure 4c), indicating good agreement between the simulated and observed spatial distributions of cloudy pixels.

In terms of the PODN metric, both schemes exhibit consistently low values below 0.5 (Figure 4d), indicating that clear-sky scenes are frequently misclassified as cloudy. Nevertheless, the higher PODN values obtained with NSSL, especially for the first 24 h, indicate a better representation of clear-sky scenes compared with WSM6. The gradual decrease in PODN after 12 h is consistent with the growing discrepancy between simulated and observed clear-sky sample counts (Figures 4b and 4d). Overall, NSSL demonstrates superior skill in representing cloud occurrence, particularly in terms of spatial consistency with the observed cloud fields, whereas the WSM6 shows larger spatial displacement errors of clouds and reduced skill in discriminating between cloudy and clear-sky conditions during the spin-up period.

Table 3. Contingency table for binary cloud-amount forecast accuracy metrics

	Model Cloud (Mcloud)	Model Clear (Mclear)
Obs Cloud (Ocloud)	Na (Hits)	Nc (Misses)
Obs Clear (Oclear)	Nb (False Alarms)	Nd (Correct Negatives)

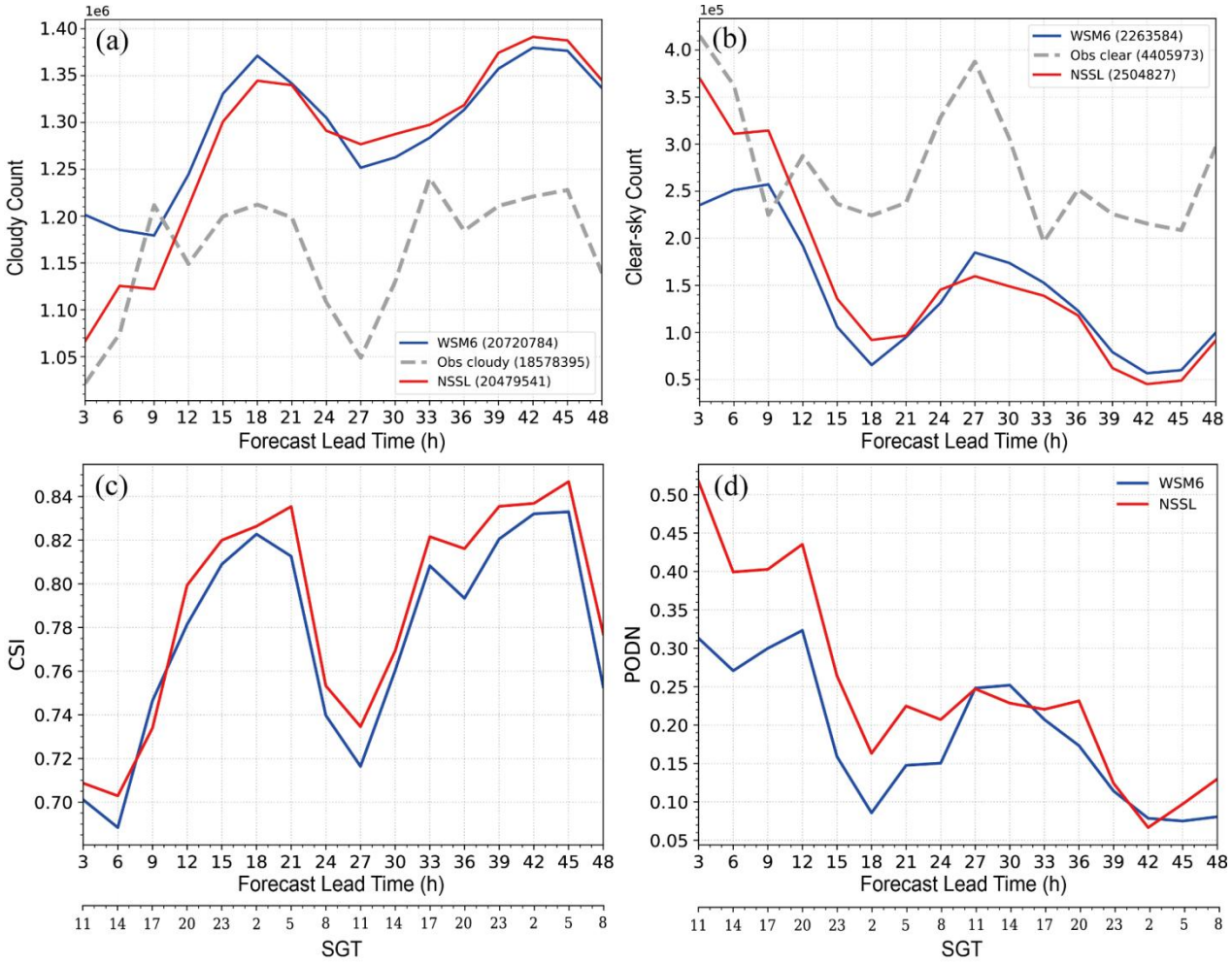


Figure 4. Observed and model-simulated (a) cloudy and (b) clear-sky pixels counts, along with (c) Critical Success Index (CSI) for cloud-amount forecast and (d) Probability of Detection for Non-cloud (PODN) as a function of forecast lead time. The forecasts are initialized at 00:00 UTC and the corresponding Singapore local times are also marked in the x-axis

The brightness temperature difference (BTD) of the ~8.5–8.7 μm minus the ~11 μm window channels can be used to effectively discriminate liquid and ice clouds because of differences in their radiative properties (Otkin et al., 2009; Menzel et al., 2015). Figure 5 illustrates the joint frequency distributions of the BTD of 8.6–11.2 μm ($BTD_{8.6\text{-}11.2}$) versus the 11.2 μm BT in the observations and model simulations for several distinct liquid- and ice-cloud types. During the study period, liquid-water clouds identified by AHI retrievals are relatively rare, accounting for ~5–6% of all cloudy samples, whereas ice clouds dominate, with optically thin and optically thick ice clouds comprising 45.9% and 21.2%, respectively. Supercooled liquid-water and mixed-phase clouds together account for only ~1–2% and are therefore excluded from the analysis. The scarcity of liquid-phase cloud samples likely reflects an inherent limitation of passive infrared sensors, which are primarily sensitive to the uppermost cloud layer, such that liquid clouds may be obscured by overlying ice clouds and are therefore underrepresented in IR-based cloud-type retrievals (Haynes et al., 2022).

The observed frequency distribution exhibits a high-frequency core (> 1.0%) spanning BTs of 200-290 K and $BTD_{8.6\text{-}11.2}$ from −4 K to 5 K (Figures 5a-c). The positive $BTD_{8.6\text{-}11.2}$ value corresponds to ice-phase clouds, resulting from the reduced emissivity of ice particles at 11.2 μm relative to 8.6 μm (Figures 5b-c). In contrast, liquid water clouds generally yield $BTD_{8.6\text{-}11.2} < 0$ with 11.2 μm BTs in the range of 240-290 K, reflecting their higher emissivity at 11.2 μm compared with 8.6 μm (Figure 5a). Moreover, under cloudy conditions, lower 11.2 μm BTs (< 240 K) indicate optically thicker clouds or higher altitude clouds, often associated with deep convection, whereas higher BTs (> 260 K) generally correspond to optically thinner or lower altitude clouds.

Relative to the observations, the overall BTD–BT pattern in the low-frequency regime (< 1.0%) is noticeably broadened in both schemes (Figures 5d-i), indicating increased uncertainty in the prediction of low-frequent cloud states. The extended $BTD_{8.6\text{-}11.2}$ tails exceeding 15 K in both simulations are likely associated with the presence of semi-transparent ice clouds, which amplify extinction differences between 8.6 and 11.2 μm (Mayer et al., 2024). Besides, the ice cloud distribution produced by WSM6 is systematically shifted toward larger positive BTDs when the observed peak occurrence falls within ~200–260 K of 11.2 μm BTs and -5–0 K of BTDs (Figures 5b-c and 5e-f), suggesting biases in the simulated optical and microphysical properties of those ice clouds.

In the high-frequency core (frequency > 1.0%), both schemes reproduce the observed BTD distribution of liquid-water clouds reasonably well, although the frequency of colder liquid-water cases (BT < 280 K) remains underestimated (Figures 5a, 5d, and 5g). It is also noted that WSM6 overpredicts the frequency within the 0–5 K BTD range (Figure 5d), which may be attributable to misclassification between liquid- and ice-phase cloud categories. For optically thin ice clouds, WSM6 more accurately reproduces the observed frequency structure within the BT range of 220–290 K and BTDs of −2 to 5 K (Figures 5b and 5e). In contrast, NSSL overpredicts the occurrence of thin-ice-cloud cases with BTs below 230 K (Figures 5b and 5h). This higher occurrence of high-level ice-cloud cases is also reflected in the enhanced frozen hydrometeor content and larger cloud fraction above 200 hPa in NSSL (Figure 8). Despite these differences, both schemes show better performance for optically thin ice clouds than for the other ice-cloud regimes. Under thick-ice conditions, both simulations underpredict the observed frequencies (Figures 5c, f, and i), with WSM6 showing a larger bias than NSSL within the 200–220 K BT range. This relatively greater underprediction in WSM6 may be associated with its lower cloud-ice, snow contents and reduced cloud fraction in the upper troposphere, despite its higher graupel content in the middle troposphere (Figure 8). In this study, “thick” and “thin” ice clouds refer to optically thick and optically thin categories defined by the AHI L2 cloud-type product based on optical properties, rather than geometric thickness. The anomalously warm simulated BTs (>280 K) under observed thick-ice-cloud conditions in both schemes (Figures 5f and 5i) may reflect spatial mismatches between observed and simulated cloud structures, and/or insufficient ice condensate. These deficiencies may reduce cloud infrared opacity, allowing greater contributions from warmer lower atmospheric layers and the surface to the simulated radiances, thereby increasing BTs. Furthermore, the similar model simulated BT-BTD distributions for optically thin and thick ice clouds, in contrast to the distinct observed distributions, suggest that both microphysics schemes may have limitations in reproducing the distinct radiative characteristics of these two cloud regimes. Uncertainties in the treatment of ice-cloud scattering in the radiative

transfer calculations may also contribute to these simulation errors (Okamoto, 2017). Overall, the phase-dependent structure in BTD space is generally in good agreement between the observations and both schemes, whereas larger discrepancies are evident along the BT axis, implying greater uncertainties in the prediction of cloud-top characteristics than in the split-window radiative response.

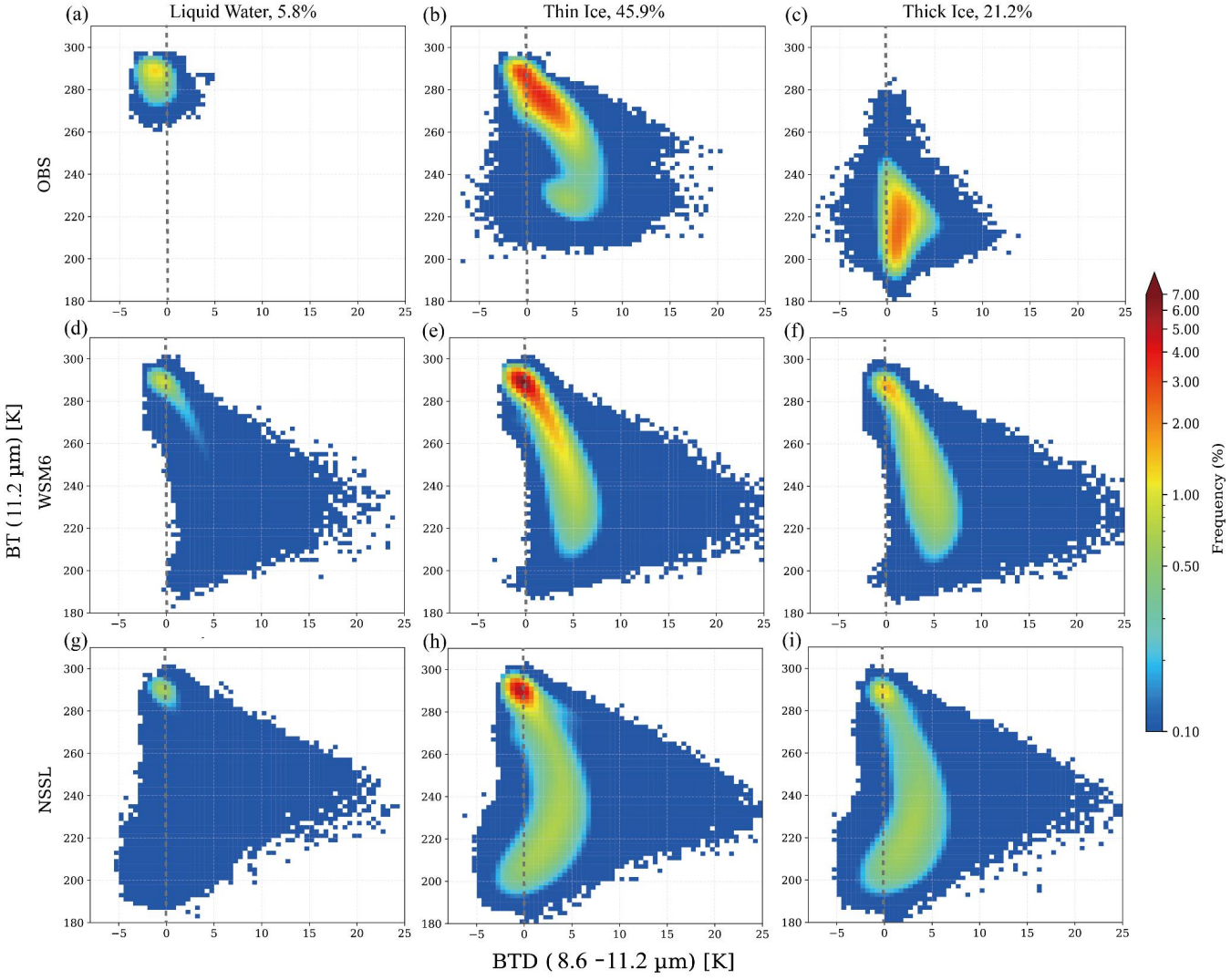


Figure 5. Frequency distributions (> 0.1%) of 8.6–11.2 μm (channel 11–14) brightness temperature differences (BTDs, units: K) versus 11.2 μm (channel 14) brightness temperatures (BTs, units: K) under different AHI L2 cloud-type conditions, including liquid water clouds (first column), thin ice clouds (second column), and thick ice clouds (third column), shown for (a-c) observations, (d-f) WSM6 simulations, and (g-i) NSSL simulations. Statistics are calculated using cloud-matched samples and binned at 0.5 K intervals for BTD and 2 K intervals for BT, based on 24-48 h forecasts with a 6 h interval.

Figure 6 presents the joint frequency distributions of cloud-top pressure (CTP) versus the cloud-top sensitive AHI channel 16 BTs for the observations and for the WSM6 and NSSL simulations. In the model, cloud top is diagnosed following the methodology of the ECMWF Integrated Forecasting System (ECMWF, 2024) and is defined as the uppermost level of

consecutive cloudy layers within each column. The observed cloud-top height is obtained from the Himawari-9 AHI Level-2 cloud-height product and represents a radiatively retrieved cloud-top height derived from multispectral infrared observations. As shown in Figure 6a, the observed distribution exhibits a clear inverse relationship between CTP and BT, with higher BTs corresponding to lower cloud-top pressures. The highest observed CTP frequencies are concentrated between 150 and 350 hPa for BTs ranging from 200 to 260 K, indicative of abundant deep convective anvils. In addition, a weaker but distinct branch extends downward to layers near 900 hPa with BTs of approximately 260–270 K, representing the presence of lower-level clouds. Both WSM6 and NSSL reproduce the overall inverse CTP-BT relationship, yet exhibit systematic biases in high-cloud representation (Figures 6b-c). In both schemes, the simulated CTP frequencies are concentrated primarily between 100 and 200 hPa, with substantially fewer occurrences at 300–400 hPa than observed, indicating an overall bias toward higher cloud tops. For an infrared window channel, a higher cloud top generally shifts the effective emission level to colder atmospheric layers, resulting in a lower BT. The discrepancy is more pronounced in NSSL, which shows a higher frequency of cloud tops near 100 hPa and BTs below 220 K, consistent with its greater occurrence of thin ice clouds in the cold-BT regime (BTs < 220 K) relative to observations (Figures 5h and 5i). Meanwhile, the vertical hydrometeor distribution in NSSL shows enhanced frozen hydrometeor content and larger cloud fractions above 200 hPa (Figure 8). Additionally, WSM6 shows more pronounced BT-space biases for high-level clouds, characterized by an underprediction of colder BTs and an overprediction of warmer BTs above 200 hPa (Figure 6b), suggesting a less realistic representation of high-cloud optical properties. Furthermore, both schemes tend to underpredict the frequency of clouds below approximately 600 hPa at BTs of 260–270 K, which is generally associated with lower-level warm clouds.

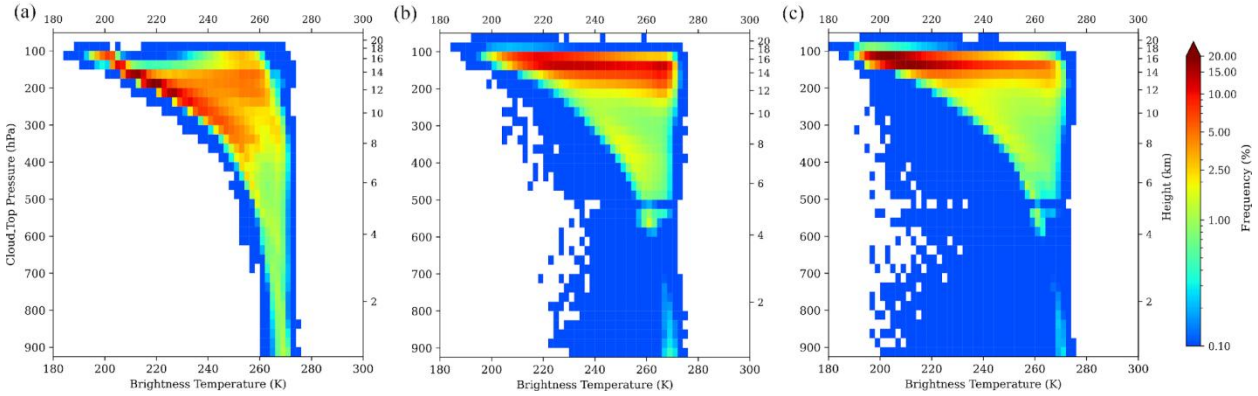


Figure 6. Frequency distributions (> 0.1%) of cloud top pressure (CTP, units: hPa) versus Channel 16 (13.3 μm) brightness temperature (BT, units: K) for (a) observations, (b) WSM6 and (c) NSSL simulations. Statistics are computed within binned intervals of 25 hPa in CTP and 2 K in BT. Model data are from 24-48 h forecasts with a 6 h interval.

3.3 Diurnal Variation of Cloud Forecast

Figure 7 displays the probability distributions of channel 13 F–O BTs as a function of forecast lead time for the WSM6 and NSSL schemes under different cloud-type conditions. To minimize the influence of model spin-up on the quantitative assessment, the first 12 h of each forecast are excluded from the analysis. The amplitude of the diurnal variation is quantified

using a first-harmonic fit with a 24-h period applied to the median F–O evolution over the 12–36 h forecast period. For liquid-water clouds (5–6 % of total cloud samples), both schemes show relatively good consistency between simulated and observed BTs. The corresponding F–O distributions are tightly centered around zero and exhibit minimal temporal variability (Figures 7a-b). For optically thin ice clouds, representing about 45% of the total samples, this category is predicted most accurately by both schemes among all ice-cloud types. This behavior is characterized by smaller F–O biases and lower standard deviations (STDs), particularly in WSM6 (Figures 7c-d). The better performance of WSM6 for optically thin ice clouds is also consistent with Figure 5, where WSM6 more closely reproduces the observed cloud-type frequency than NSSL. Under optically thick ice cloud conditions (Figures 7e – f), the contrast between the two schemes becomes more pronounced. NSSL performs substantially better, with a much smaller mean warm bias of 4.8 K compared with 26.3 K for WSM6. The larger warm bias in WSM6 (Figure 7e) is in line with its underprediction of optically thick ice cloud frequency in the cold-BT regime (Figures 5c and 5f). This behavior is further reflected in the vertical hydrometeor distributions in Figure 8, which show substantially lower upper-tropospheric cloud-ice and snow contents in WSM6 than in NSSL. Multilayered ice clouds are defined here as semitransparent upper-level ice clouds overlapping a lower opaque cloud layer (Pavolonis and Calvert, 2020). They account for 25.7% of the total cloud samples and show the lowest simulation skill in both schemes, as evidenced by broad probability plumes displaced from 0 K and the largest STDs among all cloud categories (Figures 7g-h).

The pronounced diurnal variations in F – O are evident under optically thick and multilayered ice-cloud conditions. For optically thick ice clouds, both schemes exhibit a comparable diurnal evolution, with F – O decreasing from 20:00 to 08:00 SGT and increasing thereafter toward 20:00 SGT; the corresponding amplitudes are 4.0 K for WSM6 and 2.9 K for NSSL. In contrast, the two schemes show clearly different diurnal behavior for multilayered ice clouds, with amplitudes of only 0.9 K in WSM6 but 23.5 K in NSSL. In NSSL, F–O decreases markedly from 02:00 to 14:00 SGT, followed by an increase toward nighttime. An approximately 6-h phase difference is evident between the diurnal variations of optically thick and multilayered ice clouds in NSSL. The physical-space characteristics associated with these diurnal variations are further examined in the following sections.

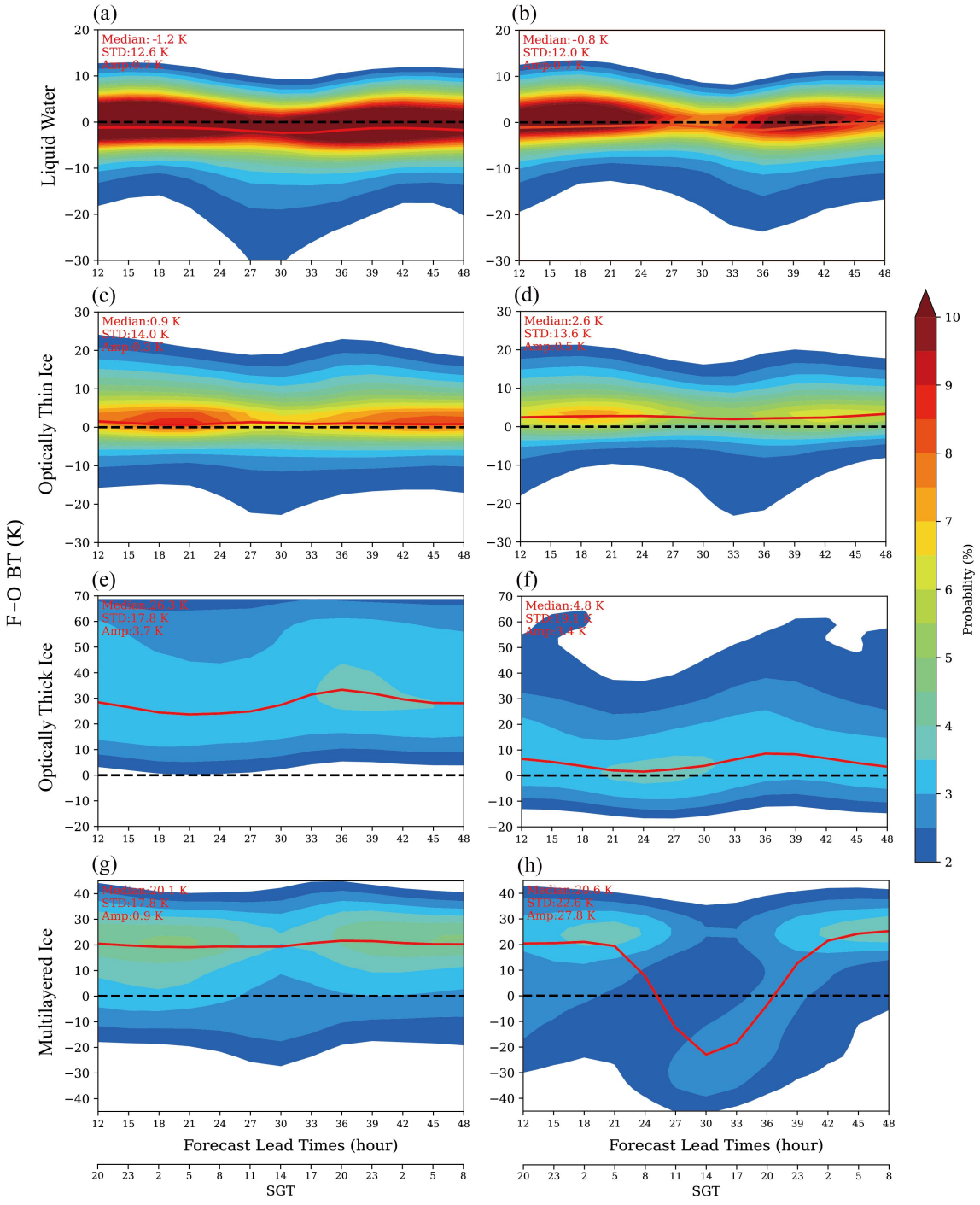


Figure 7. Probability distributions of channel 13 Forecast-Minus-Observation brightness temperature (F–O BT; units: K) as a function of forecast lead time (from 00:00 UTC) for WSM6 (first column) and NSSL (second column) under four cloud-type conditions. Lead time-averaged median, standard deviation and amplitude of F–O are shown in each legend. The red line denotes the median values at different forecast ranges.

To further elucidate the diurnal mechanisms from a microphysical perspective, Figure 8 presents the domain-averaged cloud fractions and hydrometeor mixing ratios as functions of forecast lead time and pressure level for the WSM6 and NSSL schemes. Compared with NSSL, WSM6 exhibits smaller cloud fractions (< 0.4) and thinner anvil layers between 250 and 100 hPa, whereas NSSL produces deeper anvils with larger cloud fractions (> 0.6) extending from 100 to 350 hPa (Figure 8a). Besides, a large amount of Qc in WSM6 is concentrated within the mixed-phase layer near the 273 K isotherm, exhibiting two distinct peaks during the nocturnal periods of 15–24 h and 39–48 h. Subsequently, Qc near 273 K appears to be preferentially depleted through riming and accretion processes, whereby supercooled Qc is likely collected and frozen by ice particles to enhance Qg, while Qc is possibly accreted by raindrops, leading to increased Qr. This conversion is evidenced by notable increases in Qg (up to ~0.035 g kg^{-1} between 400 and 600 hPa) and Qr (up to ~0.030 g kg^{-1} below 600 hPa). Compared with NSSL, the hydrometeor distributions in WSM6 suggest more active riming and accretion, which may be partly associated with the saturated environment (RH = 100%) surrounding mixed-phase hydrometeors near 400 hPa and the maintenance of supercooled liquid water. This contrast may also reflect a relatively high default CCN concentration in NSSL for the maritime domain, favoring more numerous but smaller cloud droplets and suppressing collision-coalescence and the associated cloud-water autoconversion. A preliminary sensitivity test was conducted with 'config_nssl_cccn' reduced from its default value of 0.8×10^9 to 0.25×10^9 m^{-3}. The results suggested more efficient warm-rain conversion, as indicated by decreased Qc and increased Qr and Qg (not shown). Moreover, the higher Qg in WSM6 may be partly attributed to its use of a shared mass-weighted fall speed for snow and graupel (Dudhia et al., 2008), which may allow graupel to remain aloft longer and contribute to the greater graupel mass loading shown in Figure 8c. Under these conditions, enhanced mid-level Qc and Qg near the melting layer (~273 K) may contribute to the reduced F–O biases and smaller STDs for liquid-water clouds in WSM6 (Figures 7a, 8a, and 8c). In contrast, upper-tropospheric Qi and Qs in WSM6 remain nearly steady, with Qi ranging from 0.005 to 0.019 g kg^{-1} and Qs generally below ~0.035 g kg^{-1} above 500 hPa (Figures 8a and 8c), values that are clearly lower than those simulated by NSSL (Figures 8b and 8d). The thinner upper-tropospheric ice layers in WSM6 may be associated with its lower relative humidity and weaker updrafts in the upper troposphere (Figures 8 and 11–12), which can limit depositional ice growth (Tao et al., 2022). This pattern is consistent with the reduced F–O biases under optically thin ice cloud conditions (Figure 7c), but also leads to systematic positive F–O biases for optically thick and multilayered ice clouds (Figures 7e and 7g). Similarly, Grasso et al. (2014) reported that excessive Qc-to-Qg conversion reduces the primary source of anvil ice mass. In contrast to WSM6, the saturation layer in NSSL is positioned at a higher altitude (~250 hPa), accompanied by enhanced concentrations of Qi (~0.034 g kg^{-1}) and Qs (~0.078 g kg^{-1}) extending through the 350–150 hPa layer (Figures 8b and 8d). This tendency is consistent with previous MPAS- and WRF-based evaluations showing larger cloud-ice mixing ratios in NSSL than in WSM6 (Chen et al., 2026; Morrison et al., 2015). The enhanced ice condensate may partly contribute to the smaller F–O biases for optically thick ice clouds in NSSL, whereas a relatively large positive bias persists for optically thin ice-cloud scenes (Figures 7d and 7f). Moreover, the greater abundance of high-level thin ice clouds in NSSL shown in Figure 8b is closely associated with substantially higher frequencies of thin-ice scenes at cold BTs below ~240 K (Figure 5h) and a higher frequency of cold-cloud tops near 100 hPa than observed (Figure 6c).

The stronger diurnal variability of F–O in NSSL under multilayered ice-cloud conditions (Figure 7) coincides with larger diurnal variations in upper-tropospheric ice-phase hydrometeors (Qi and Qs) between approximately 300 and 100 hPa (Figures 8b and 8d). During the daytime convective period (14:00–17:00 SGT), enhanced upper-level cloudiness and larger Qi and Qs in NSSL are associated with colder simulated BTs and more negative F−O values (Figure 7h). In contrast, the nighttime reduction in ice-phase hydrometeor contents is accompanied by a shift toward more positive F–O values (Figures 7h, 8b, and 8d). For optically thick ice clouds, however, WSM6 exhibits a relatively large diurnal amplitude of F−O than NSSL (Figure 7e). This variation appears to be associated with larger diurnal changes in Qc and Qg, with higher hydrometeor contents during 23:00–05:00 SGT corresponding to reduced positive F–O biases, whereas lower hydrometeor contents during 17:00–23:00 SGT coincide with increased positive biases (Figures 8a and 8c). Furthermore, the larger variations in F–O bias with broader, lower-frequency distributions during 11:00 – 17:00 SGT appear to be associated with enhanced hydrometeor contents, suggesting more active cloud microphysical evolution during the daytime. In contrast, the nighttime period of 20:00–05:00 SGT is characterized by weaker F−O variability and more persistent high-frequency distributions, together with generally reduced hydrometeor contents and potentially weaker cloud microphysical activity.

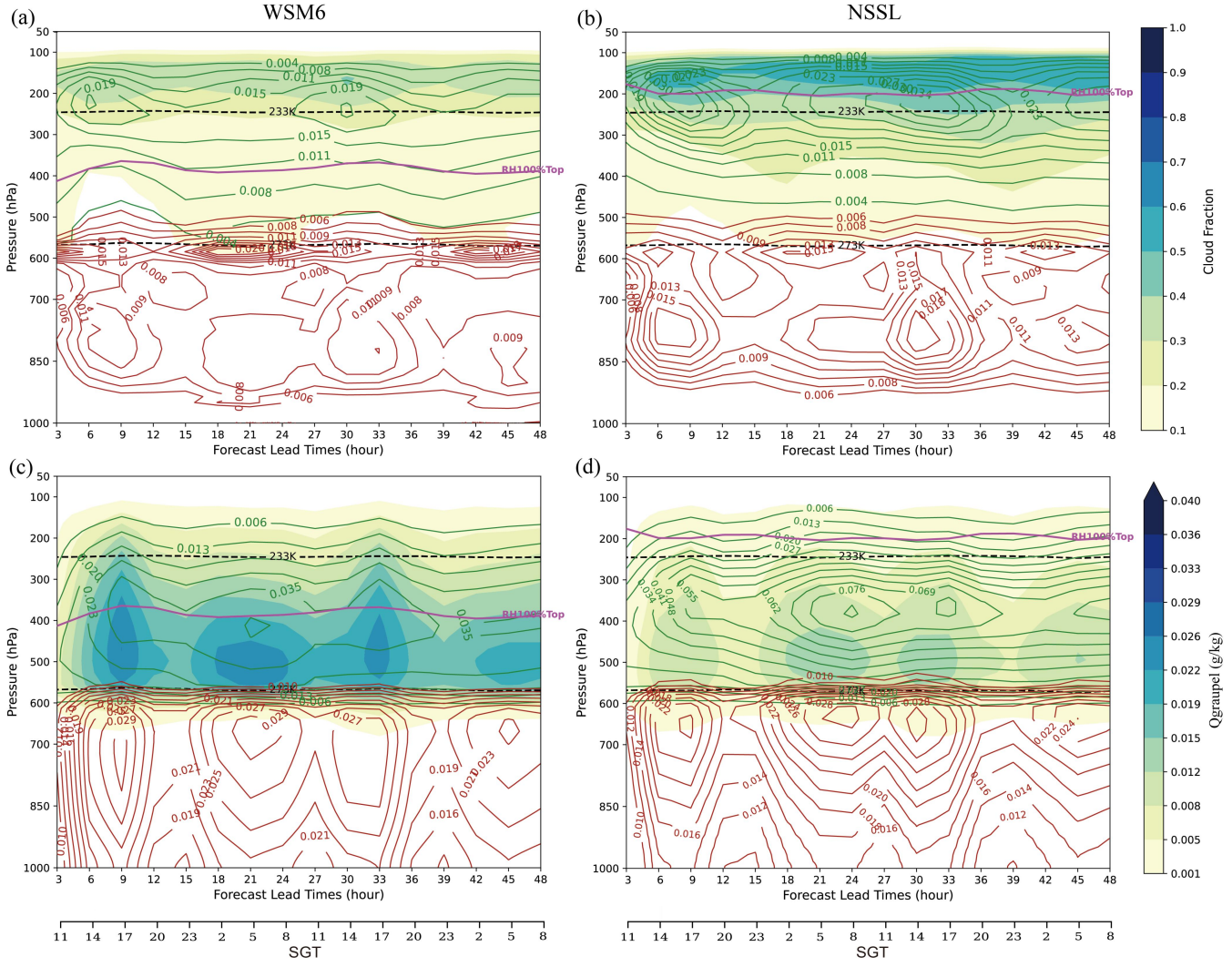


Figure 8. Domain-averaged (a, b) cloud fraction (shading), the mixing ratio (units: g/kg) of Qc (red contours) and Qi (green contours), and (c, d) Qg (shading), Qs (green contours) and Qr (red contours) as a function of forecast lead time and pressure for the WSM6 (first column) and NSSL (second column) microphysics schemes. The dashed black lines mark the 273 K and 233 K isotherms, and the magenta line indicates the uppermost level where the relative humidity reaches 100%.

To evaluate the spatial characteristic of diurnal variations, Figure 9 presents the daytime and nighttime horizontal distributions of F–O BTs for AHI channel 13, averaged within 1° × 1° longitude–latitude bins. During the daytime, both schemes exhibit a distinct land-sea contrast, with predominantly negative F–O biases over land and positive biases over the adjacent oceans. Overall, this land-sea contrast is more pronounced in NSSL, reaching approximately 40–50 K, with cold biases of about -30 K over land and warm biases of roughly 15 K over nearby oceans (Figure 9b). In comparison, WSM6 produces a weaker contrast of roughly 20–40 K, characterized by smaller cold biases over land but stronger warm biases over the ocean (Figure 9a), which are further examined in Figures 10a and 11a. As shown in Figures 9c-d, the negative daytime F–

O biases over land shift markedly toward positive values (~5–20 K) at night for both schemes, indicating weakened convection and reduced cloud amounts after sunset. In particular, over land, the NSSL scheme exhibits a larger diurnal range in F–O (~15–30 K) than WSM6 (~10–25 K). Over the ocean, both schemes show substantially weaker diurnal variability, with NSSL producing more negative F–O biases up to -20 K and WSM6 yielding predominantly positive biases ranging from 10 to 25 K (Figures 9c-d).

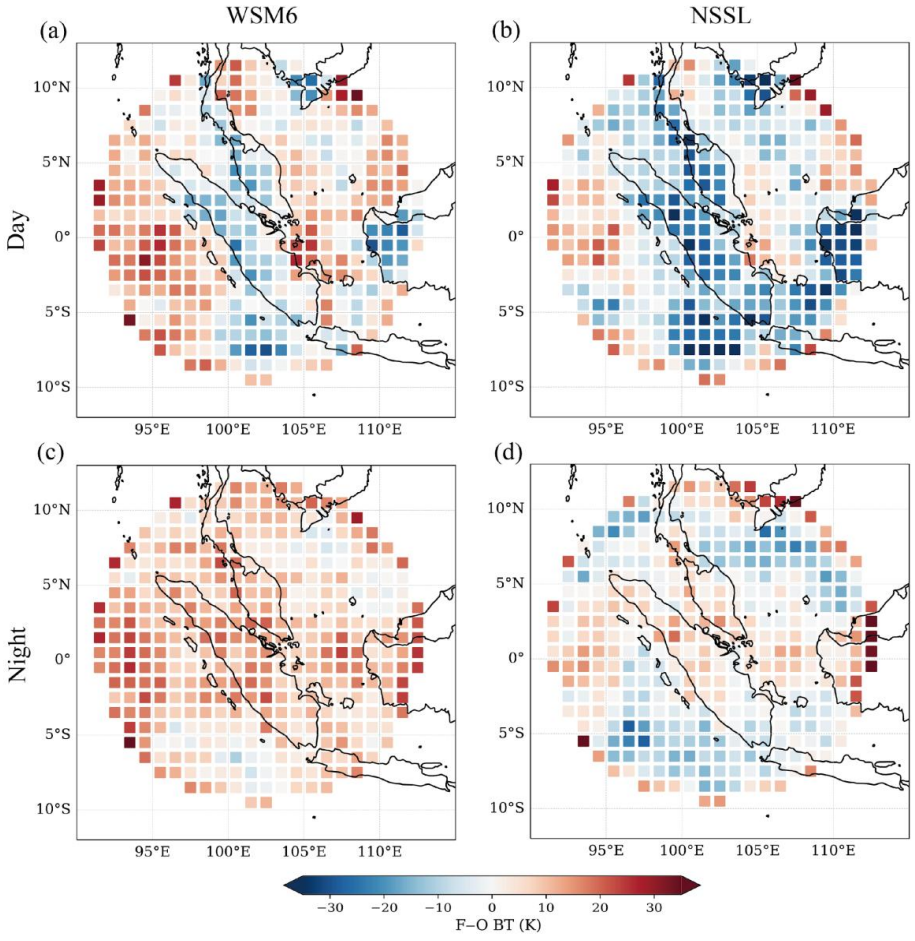


Figure 9. Spatial distributions of the averaged Forecast-Minus-Observation (F–O, units: K) for Himawari-9 channel-13 brightness temperatures, computed within 1° × 1° longitude–latitude bins, during (a, b) the local daytime 11:00-17:00 SGT from a forecast range of 3-9 h and 27-33 h and (c, d) the local nighttime 21:00-03:00 SGT from a forecast range of 13-19 h and 37-43 h for the WSM6 (left) and NSSL (right) schemes.

To further examine the influence of topography and atmospheric environments on cloud diurnal evolution, Figures 10-11 present daytime- and nighttime-averaged cross-sections of simulated cloud fraction, vertical velocity, and thermodynamic fields along the S1 and S2 transects shown in Figure 1. The averages are calculated from forecast samples within the corresponding daytime (11:00–17:00 SGT) and nighttime (21:00–03:00 SGT) periods.

Following Yokoi et al. (2017) and Okugawa et al. (2024), the S1 cross section shown in Figure 10 spans different terrain types and is oriented approximately normal to the Sumatra mountain range (Barisan Mountains), where the terrain rises to elevations of approximately 1 km. During the daytime, both schemes exhibit enhanced positive potential temperature anomalies around the elevated terrain, accompanied by strong vertical motions and extensive cloud coverage between 400 and 100 hPa (Figures 10a-b). This pronounced convective development over the mountainous region is consistent with Okugawa et al. (2024), who suggested that daytime solar heating, land-sea circulation, and orographic forcing may favor vigorous convection over Sumatra land, particularly promoting upper-level ice-cloud development. These daytime characteristics also help explain the larger negative F–O biases over land (Figures 9a-b), as enhanced high-level cloud coverage over the Barisan Range raises the effective infrared emission level to colder atmospheric layers, resulting in lower simulated BTs. Compared with WSM6, NSSL exhibits deeper convective updrafts over the mountain near 100° E, with enhanced vertical motion extending to higher levels and accompanied by greater upper-level cloud fraction (>0.7 above ~300 hPa). The greater amount of high-level clouds over the mountainous terrain are consistent with the larger negative F–O biases in Figure 9b. In contrast, over the low-elevation marine regions, negative potential temperature anomalies are accompanied by relatively weak updrafts and reduced upper-level cloud development (Figures 10a-b), consistent with the positive F–O biases in both schemes (Figures 9a-b). The weaker upper-tropospheric ascent in WSM6 compared with NSSL may be partly related to its enhanced graupel content shown in Figure 8, as increased hydrometeor loading can reduce net buoyancy and thereby suppress updraft development (Conrick et al., 2018). It is also noteworthy that NSSL produces greater upper-tropospheric cloud coverage than WSM6 over both land and ocean, consistent with the larger amounts of high-level ice-phase hydrometeors shown in Figure 8.

After sunset, the thermodynamic and cloud structures over the adjacent seas show relatively weak diurnal variations, consistent with the small day-night differences in F–O biases. Over the mountainous region (~100°–103° E), however, the cross-sectional structure exhibits pronounced diurnal differences. Specifically, both schemes exhibit larger positive F–O biases over the mountainous region (Figures 9c–d), coinciding with weaker upward motion and reduced upper-level cloud amount at night (Figures 10c–d). Notably, the larger nighttime positive bias in WSM6 is consistent with the scarcity of cloud cover above 300 hPa (Figure 10c). The pronounced day–night contrast over the mountainous terrain may be attributed to the terrain-modulated diurnal cycle of surface heating and local circulation. During the daytime, enhanced solar heating over elevated terrain can strengthen upslope flow and convective instability, thereby promoting cloud development (Hartmann et al., 2018; Pepin et al., 2022). At night, radiative cooling stabilizes the lower atmosphere and weakens thermally driven upslope circulation, resulting in reduced vertical motion and suppressed convective cloud development over the mountains (Sokol et al., 2020).

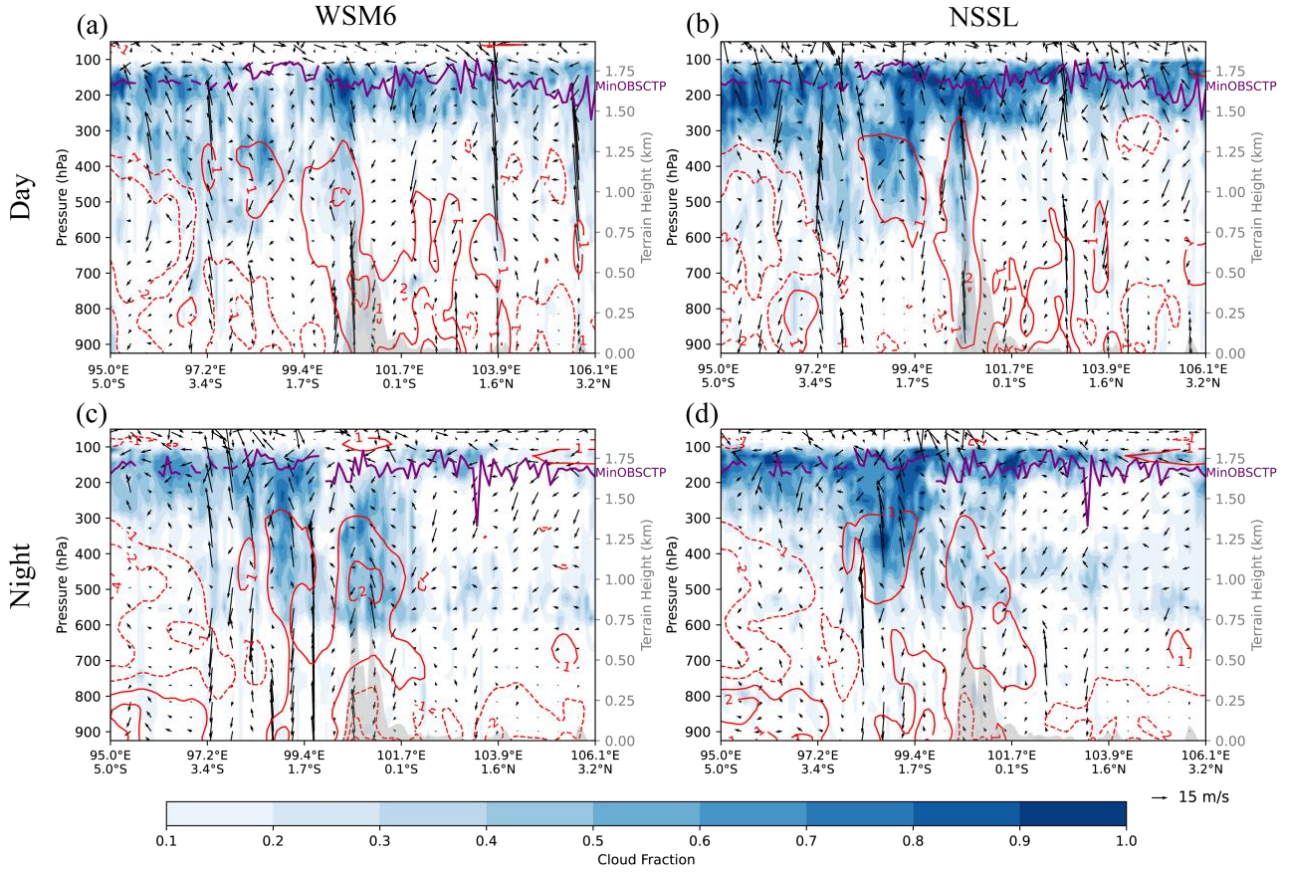


Figure 10. Daytime- and nighttime-averaged cross-sections of the cloud fraction (blue-filled contours), vertical velocity (black vectors; units: m/s), equivalent potential temperature anomaly (red contours; units: K), minimum observed cloud-top pressures (purple lines; units: hPa) and terrain height (grey shading; units: km) along the S1 transect shown in Figure 1 for the (a, b) 11:00-17:00 SGT daytime from a forecast range of 3-9 h and 27-33 h and (c, d) 21:00-03:00 SGT nighttime from the 13-19 h and 37-43 h forecasts in WSM6 (first column) and NSSL (second column) experiments.

The S2 transect crosses a region where the two simulations exhibit distinct differences in the diurnal variation of F−O and spans the land-sea transition from the eastern Indian Ocean to western Java. The variations in near-surface temperature (T2 m) and specific humidity (Q2 m) along this transect further characterize the contrasting thermodynamic conditions (Figures 11a-b). Over the ocean (~99–100° E and ~101.8–102.5° E), T2 m remains nearly constant at around 301 K, whereas inland temperatures near 100.4° E and 101.8° E increase from nighttime to daytime by approximately 2–8 K in both schemes (red curves in Figures 11a-b), reflecting enhanced daytime shortwave heating and nighttime longwave radiative cooling over land. Meanwhile, the daytime-minus-nighttime difference in Q2 m shows an increase of about 1–3 $g \cdot kg^{-1}$ from the ocean toward inland regions (blue curves in Figures 11a-b). This enhanced land–sea thermodynamic gradient appears to strengthen vertical motion along the coastal interface and promote convective development extending to above ~200 hPa (Figures 11c-f). In contrast to the pronounced land-based diurnal variability, the adjacent coastal oceans maintain relatively stable thermodynamic conditions, primarily due to the greater heat capacity and thermal inertia of seawater compared with land.

Therefore, the amplified land–sea thermodynamic contrast appears to facilitate vigorous cloud evolution over land and adjacent coastal regions, with cloud fractions frequently exceeding 0.7 between 100 and 300 hPa during the daytime (Figures 11c-d), followed by rapid nocturnal subsidence and dissipation to below ~300 hPa (Figures 11e-f). Consequently, the deeper and higher clouds developing over land during the daytime are associated with more negative F–O biases (Figures 9a-b), as increased cloud optical thickness elevates the effective infrared radiating level to colder cloud tops, resulting in lower simulated BTs. Likewise, rapid cloud dissipation over land at night corresponds to pronounced positive F–O biases. Over the ocean, the relatively stable near-surface thermodynamic environment, together with weaker convective instability, maintains cloud fractions at more steady levels (~0.3–0.6) above ~400 hPa during both daytime and nighttime. This may explain the persistence of some negative F–O biases over the ocean within 102.0–102.5° E and 6.0–9.0° N throughout the diurnal cycle (Figure 9). Furthermore, compared with WSM6, the larger diurnal F–O amplitude produced by NSSL over land (Figures 9b and 9d) is likely related to its simulation of stronger upper-tropospheric vertical motion around 100-300 hPa (Figures 10 and 11), which may enhance the diurnal evolution of Qi and Qs in high-level clouds through lofting and sedimentation processes.

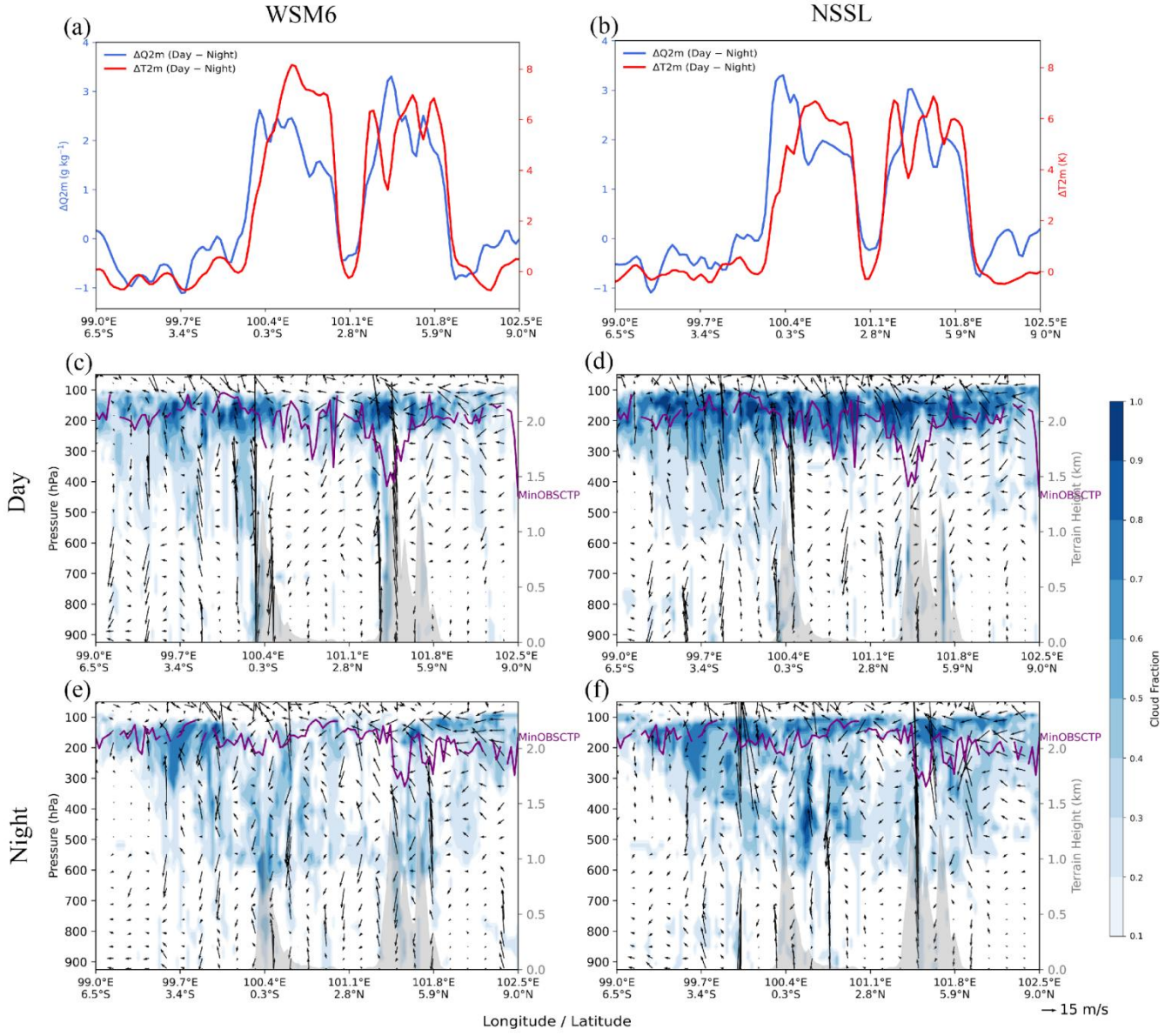


Figure 11. Vertical cross-sections of daytime-minus-nighttime differences in (a, b) 2 m specific humidity (blue lines; units: g kg^{-1}) and 2 m temperature (red lines; units: K) along the S2 transect shown in Figure 1, together with simulated cloud fraction (blue-filled contours), vertical velocity (black vectors; units: m s^{-1}), minimum AHI L2 cloud-top pressure (purple contours; units: hPa), and terrain height (grey shading; units: km) during (c, d) 11:00-17:00 SGT daytime from a forecast range of 3-9 h and 27-33 h and (e, f) 21:00-03:00 SGT nighttime from the 13-19 h and 37-43 h forecasts simulated by the WSM6 (first column) and NSSL (second column) microphysics schemes.

4 Summary

Tropical cloud prediction over the Maritime Continent remains a persistent challenge for numerical weather prediction models, as forecast performance is strongly constrained by uncertainties in microphysical parameterizations under complex terrain and

atmospheric conditions. To support model development for cloud prediction over this region, Himawari-9 AHI multi-band radiances together with Level-2 cloud products are jointly used to evaluate the tropical cloud characteristics simulated by MPAS using the WSM6 and NSSL microphysics schemes. The proposed infrared-radiance-based framework is further designed to exploit these high-resolution satellite observations more effectively for model assessment. The main findings are summarized below.

The evaluation using multi-band AHI radiance data shows that WSM6 more accurately represents the observed BT range in the water-vapor bands, whereas NSSL better represents cold BTs in cloud-sensitive window channels. For the window channels, the larger positive F–O departures in WSM6 generally coincide with higher OLR and lower CIWP, whereas the smaller positive departures in NSSL are associated with lower OLR and larger CIWP. These differences suggest that NSSL tends to produce more extensive upper-level ice-cloud coverage than WSM6.

The cloud-amount evaluation with AHI cloud mask retrievals suggests that NSSL achieves higher skill in representing overall cloudiness, particularly in the spatial placement of cloudy pixels. However, the WSM6 simulations exhibit larger spatial displacement errors and tend to overestimate cloud fraction by misclassifying clear-sky pixels as cloudy during the model spin-up period. In terms of vertical cloud structure, both schemes tend to overpredict the cloud-top heights for high-level clouds while underpredicting the occurrence of mid- and low-level clouds relative to observations. Similar biases have been reported in previous WRF microphysics evaluations, where cloud-top heights are generally overestimated, potentially linked to an overabundance of upper-level cloud ice (Zhu et al., 2023), whereas mid-level cloudiness appears to be underestimated (Jankov et al., 2011). The cloud-top biases may also be partly related to the 3-km grid spacing, as relatively coarse kilometer-scale grids can produce larger convective cells with reduced entrainment of midlevel environmental air, thereby favoring higher cloud tops (Bryan and Morrison, 2012).

The AHI cloud-type diagnostics further indicate that WSM6 tends to underpredict the frequency of cold ice clouds, leading to systematic warm biases in F–O. This tendency is consistent with previous findings that suggest an underrepresentation of upper-level ice clouds in WSM6 (Grasso et al., 2014). The biases are likely associated with limited development of solid-phase hydrometeors under conditions of weaker updrafts and lower relative humidity in the upper troposphere. In contrast, NSSL produces more abundant ice and snow hydrometeors above ~400 hPa within higher saturation layers and stronger upper-level ascent, resulting in smaller F–O for optically thick ice clouds. However, NSSL tends to overpredict the frequency of thin-ice clouds in the upper troposphere. Despite these differences, both schemes exhibit relatively higher predictive skill for liquid-water and optically thin ice clouds than for other cloud types. In contrast, optically thick ice and multilayer ice clouds are associated with the largest forecast errors in WSM6 and NSSL, respectively, with NSSL showing the largest diurnal amplitude of F–O in multilayer ice cloud conditions.

Moreover, both schemes exhibit pronounced cloud-related diurnal variations in F–O over land. Negative departures during the daytime suggest an overestimation of cloud-top height and/or high-cloud amount. At night, F–O shifts to positive values, likely reflecting an underestimation of high-level or optically thick clouds. This behavior is likely driven by diurnal heating–cooling asymmetry over complex terrain associated with surface radiative forcing. The land–sea thermodynamic contrast may

further enhance cloud development over land and adjacent coastal regions. Based on Himawari-8 AHI observations over East Asia and the Tibetan Plateau, Chen et al. (2018) likewise found that the diurnal amplitude of cloudiness is larger over land than over ocean and tends to increase over complex terrain. Compared with WSM6, the relatively large diurnal F–O amplitude in NSSL is consistent with its more pronounced diurnal variability in upper-tropospheric ice-phase hydrometeors.

The above findings highlight several directions for future development in both model forecasting and all-sky infrared radiance assimilation. On the modelling side, improving the representation of ice-phase hydrometeor partitioning is essential for better distinguishing among optically thick, thin, and multilayer ice clouds. The simulated BT differences between WSM6 and NSSL may reflect not only differences in their underlying microphysical formulations but also the strong sensitivity of cloud microphysical processes to parameter settings, particularly those governing upper-level ice clouds. Future work could additionally incorporate direct observations of cloud-ice fall speeds and vertical cloud structure from the EarthCARE satellite to provide more physically based constraints for evaluating and improving cloud microphysics parameterizations (Illingworth et al., 2015; Wehr et al., 2023). In addition, more accurate simulation of upper-tropospheric dynamical and thermodynamic conditions (e.g., upper-level winds, supersaturation, and vertical transport of condensate) is crucial for reducing cloud-top height biases. Over the Maritime Continent, improved representations of land-surface meteorological processes and terrain effects may further improve the simulation of tropical cloud diurnal evolution. From the data assimilation perspective, applying cloud-type-dependent bias correction or quality-control strategies within the all-sky infrared assimilation framework may improve performance under specific cloud regimes. Future all-sky assimilation experiments would also benefit from incorporating diurnally varying hydrometeor background-error structures to better capture pronounced day–night contrasts. Moreover, targeted observing-system experiments that select infrared channels according to cloud-regime sensitivities and microphysics-scheme-dependent simulation characteristics may help optimize the use of Himawari-9 radiances in tropical cloud assimilation. Despite the insights gained from the present experiments, several limitations remain. The current results are based on a limited number of cases and time periods, and their robustness would benefit from evaluation using longer time series and a broader range of weather systems. In addition, future studies could incorporate additional observational datasets, such as radar and microwave measurements, to enable a more comprehensive assessment of sub-cloud and in-cloud microphysical properties.

Code and Data Availability

The source code of MPAS-JEDI version 3.0.3 is archived on Zenodo at https://doi.org/10.5281/zenodo.19209009 (last access: 10 June 2026; JCSDA and NCAR, 2025). The modified MPAS-Atmosphere v8.2.2 code used in this study and CRTM v2.4.1 are available via Zenodo at https://doi.org/10.5281/zenodo.23487937 (last access: 10 June 2026; Zhang et al. 2026c) and https://doi.org/10.5281/zenodo.7823722 (last access: 10 June 2026; Johnson et al., 2023), respectively. All model configuration files, data processing codes, and auxiliary scripts required to reproduce the results of this study are publicly available on Zenodo at https://doi.org/10.5281/zenodo.19925596 (last access: 10 June 2026; Zhang et al., 2026a). The

ECMWF HRES data, provided by the Centre for Climate Research Singapore (CCRS) under the NCAR–CCRS collaborative project, are subject to third-party access and redistribution restrictions, and access requests should be directed by email to the corresponding author. The processed Himawari-9 AHI observation data used in this study have been archived on Zenodo at https://doi.org/10.5281/zenodo.20312122 (last access: 10 June 2026; Zhang et al., 2026b). The model output data are available from the corresponding author upon request due to their large volume.

Author contributions

X.Z. and L.J. developed the verification methods. X.Z. conducted the experiments, performed the testing and validation, and prepared the manuscript. L.J. and Z.L. contributed to additional testing and validation of the datasets and results. Z.L. also provided valuable feedback on the development and implementation of the verification procedures, as well as on the manuscript. T.S., W.W., and I.-H.C. provided technical assistance and offered scientific suggestions that helped improve the study. All authors have read and agreed to the published version of the manuscript.

Competing interests

The contact author has declared that none of the authors has any competing interests.

Disclaimer

Publisher's note: Copernicus Publications remains neutral with regard to jurisdictional claims made in the text, published maps, institutional affiliations, or any other geographical representation in this paper. While Copernicus Publications makes every effort to include appropriate place names, the final responsibility lies with the authors. Views expressed in the text are those of the authors and do not necessarily reflect the views of the publisher.

Acknowledgements

The authors gratefully acknowledge the SINGV-NG team from both the National Center for Atmospheric Research and the Centre for Climate Research Singapore (CCRS) for their dedicated collaboration in the development of the system. We also acknowledge the Computational and Information Systems Laboratory (CISL) at NSF National Center for Atmospheric Research (NCAR) for their technical support.

Financial support

This research was supported by the Centre for Climate Research Singapore (CCRS) of the Meteorological Service Singapore.

References

Aslam, A. A.: Rainfall over the Maritime Continent: key processes, scale interactions and model representation. Weather, 80, 176–185, https://doi.org/10.1002/wea.7731, 2025.

Atlas, R. L., Bretherton, C. S., Sokol, A. B., Blossey, P. N., and Khairoutdinov, M. F.: Tropical cirrus are highly sensitive to ice microphysics within a nudged global storm-resolving model, *Geophys. Res. Lett.*, 51, e2023GL105868, https://doi.org/10.1029/2023GL105868, 2024.

Aumann, H. H., Chen, X., Fishbein, E., Geer, A., Havemann, S., Huang, X., and Coauthors: Evaluation of radiative transfer models with clouds, *J. Geophys. Res. Atmos.*, 123, 6142–6157, https://doi.org/10.1029/2017JD028063, 2018.

Battaglia, A., Kollias, P., Dhillon, R., Roy, R., Tanelli, S., Lamer, K., and Coauthors: Spaceborne cloud and precipitation radars: Status, challenges, and ways forward, *Rev. Geophys.*, 58, e2019RG000686, https://doi.org/10.1029/2019RG000686, 2020.

Bessho, K., and Coauthors: An introduction to Himawari-8/9—Japan's new-generation geostationary meteorological satellites, *J. Meteor. Soc. Japan*, 94, 151–183, https://doi.org/10.2151/jmsj.2016-009, 2016.

Bryan, G. H. and Morrison, H.: Sensitivity of a simulated squall line to horizontal resolution and parameterization of microphysics, *Mon. Weather Rev.*, 140, 202–225, https://doi.org/10.1175/MWR-D-11-00046.1, 2012.

Centurioni, L. R., and Coauthors: Global in situ observations of essential climate and ocean variables at the air–sea interface, *Front. Mar. Sci.*, 6, 419, https://doi.org/10.3389/fmars.2019.00419, 2019.

Chang, C., Lu, M., and Lim, H.: Monsoon convection in the Maritime Continent: Interaction of large-scale motion and complex terrain, *Meteor. Monogr.*, 56, 6.1–6.29, https://doi.org/10.1175/AMSMONOGRAPHS-D-15-0011.1, 2016.

Chen, D., Guo, J., Wang, H., Li, J., Min, M., Zhao, W., and Yao, D.: The cloud top distribution and diurnal variation of clouds over East Asia: preliminary results from Advanced Himawari Imager, *J. Geophys. Res. Atmos.*, 123, 3724 – 3739, https://doi.org/10.1002/2017JD028044, 2018.

Chen, I.-H., Patel, P., Furtado, K., Wang, W., Liu, Z., Barker, D., Dudhia, J., Zhang, H.: Performance evaluation of regional weather predictions with the Model for Prediction Across Scales – Atmosphere (MPAS-A) over the Maritime Continent. *Q. J. R. Meteorol. Soc*, e70129, https://doi.org/10.1002/qj.70129, 2026.

Chen, Y., Weng, F., Han, Y., and Liu, Q.: Validation of the community radiative transfer model using CloudSat data, *J. Geophys. Res.*, 113, D00A03, https://doi.org/10.1029/2007JD009561, 2008.

Cho, H., Jun, S. Y., Ho, C. H., and McFarquhar, G.: Simulations of winter Arctic clouds and associated radiation fluxes using different cloud microphysics schemes in the Polar WRF: Comparisons with CloudSat, CALIPSO, and CERES, *J. Geophys. Res. Atmos.*, 125, https://doi.org/10.1029/2019JD031413, 2020.

Chow, W. T. L., Cheong, B. D., and Ho, B. H.: A multimethod approach towards assessing urban flood patterns and its associated vulnerabilities in Singapore, *Adv. Meteorol.*, 2016, 7159132, https://doi.org/10.1155/2016/7159132, 2016.

Cintineo, R., Otkin, J., Xue, M., and Kong, F.: Evaluating the performance of planetary boundary layer and cloud microphysical parameterization schemes in convection-permitting ensemble forecasts using synthetic GOES-13 satellite observations, *Mon. Weather Rev.*, 142, 163–182, https://doi.org/10.1175/MWR-D-13-00143.1, 2014.

Comin, A. N., Schumacher, V., Justino, F., and Fernández, A.: Impact of different microphysical parameterizations on extreme snowfall events in the southern Andes, *Wea. Climate Extremes*, 21, 65–75, https://doi.org/10.1016/j.wace.2018.07.001, 2018.

Conrick, R., C. F. Mass, and Q. Zhong, 2018: Simulated Kelvin – Helmholtz waves over terrain and their microphysical implications. *Journal of the Atmospheric Sciences*, 75, 2787–2800. https://doi.org/10.1175/JAS-D-18-0073.1.

Dawson, D. T., Xue, M., Milbrandt, J. A., and Yau, M. K.: Comparison of evaporation and cold pool development between single-moment and multimoment bulk microphysics schemes in idealized simulations of tornadic thunderstorms, *Mon. Weather Rev.*, 138, 1152–1171, https://doi.org/10.1175/2009MWR2956.1, 2010.

Dipankar, A., Webster, S., Sun, X., and Coauthors: SINGV: A convective-scale weather forecast model for Singapore, *Q. J. R. Meteorol. Soc.*, 146, 4131–4146, https://doi.org/10.1002/qj.3895, 2020.

Dudhia, J., Hong, S.-Y., and Lim, K.-S.: A new method for representing mixed-phase particle fall speeds in bulk microphysics parameterizations, *J. Meteorol. Soc. Jpn.*, 86A, 33-44, https://doi.org/10.2151/jmsj.86A.33, 2008.

ECMWF: IFS documentation – CY49R1, Part I: Observations, European Centre for Medium-Range Weather Forecasts, Reading, UK, available at: https://www.ecmwf.int/en/publications/ifs-documentation, 2024.

ECMWF: Medium cloud parameters, available at: https://charts.ecmwf.int/products/medium-cloud-parameters (accessed 2025).

ECMWF: Medium cloud parameters, available at: https://charts.ecmwf.int/products/medium-cloud-parameters (accessed 2025).

Feofilov, A. G., and Stubenrauch, C. J.: Diurnal variation of high-level clouds from the synergy of AIRS and IASI space-borne infrared sounders, *Atmos. Chem. Phys.*, 19, 13957–13972, https://doi.org/10.5194/acp-19-13957-2019, 2019.

Ferrier, B.: A double-moment multiple-phase four-class bulk ice scheme. Part I: Description, *J. Atmos. Sci*., 51, 249–280, https://doi.org/10.1175/1520-0469(1994)051<0249:ADMMPF>2.0.CO;2, 1994.

Franklin, C. N., Sun, Z., Bi, D., Dix, M., Yan, H., and Bodas Salcedo, A.: Evaluation of clouds in ACCESS using the satellite simulator package COSP: Global, seasonal, and regional cloud properties, *J. Geophys. Res. Atmos.*, 118, 732–748, https://doi.org/10.1029/2012JD018469, 2013.

Galligani, V. S., Wang, D., Alvarez Imaz, M., Salio, P., and Prigent, C.: Analysis and evaluation of WRF microphysical schemes for deep moist convection over south-eastern South America (SESA) using microwave satellite observations and radiative transfer simulations, *Atmos. Meas. Tech.*, 10, 3627–3649, https://doi.org/10.5194/amt-10-3627-2017, 2017.

Gehne, M., Wolding, B., Dias, J., and Kiladis, G. N.: Diagnostics of tropical variability for numerical weather forecasts, *Wea. Forecasting*, 37, 1661–1680, https://doi.org/10.1175/WAF-D-21-0204.1, 2022.

Geiss, S., Scheck, L., de Lozar, A., and Weissmann, M.: Understanding the model representation of clouds based on visible and infrared satellite observations, *Atmos. Chem. Phys.*, 21, 12273–12290, https://doi.org/10.5194/acp-21-12273-2021, 2021.

Gevorgyan, A.: Convection-permitting simulation of a heavy rainfall event in Armenia using the WRF model, *J. Geophys. Res. Atmos.*, 123, 11008–11029, https://doi.org/10.1029/2017JD028247, 2018.

Grasso, L., Lindsey, D. T., Lim, K.-S. S., Clark, A., Bikos, D., and Dembek, S. R.: Evaluation of and suggested improvements to the WSM6 microphysics in WRF-ARW using synthetic and observed GOES-13 imagery, *Mon. Weather Rev.*, 142, 3635–3650, https://doi.org/10.1175/MWR-D-14-00005.1, 2014.

Grecu, M., and Krajewski, W. F.: A large-sample investigation of statistical procedures for radar-based short-term quantitative precipitation forecasting, *J. Hydrol.*, 239, 69–84, https://doi.org/10.1016/S0022-1694(00)00360-7, 2000.

Griffin, S. M., and Otkin, J. A.: Evaluating the impact of planetary boundary layer, land surface model, and microphysics parameterization schemes on simulated GOES-16 water vapor brightness temperatures, *Atmosphere*, 13, 366, https://doi.org/10.3390/atmos13030366, 2022.

Griffin, S. M., Otkin, J. A., Rozoff, C. M., Sieglaff, J. M., Cronce, L. M., and Alexander, C. R.: Methods for comparing simulated and observed satellite infrared brightness temperatures and what do they tell us?, *Wea. Forecasting*, 32, 5–25, https://doi.org/10.1175/WAF-D-16-0098.1, 2017a.

Griffin, S. M., Otkin, J. A., Rozoff, C. M., Sieglaff, J. M., Cronce, L. M., Alexander, C. R., Jensen, T. L., and Wolff, J. K.: Seasonal analysis of cloud objects in the High Resolution Rapid Refresh (HRRR) model using object-based verification, *J. Appl. Meteor. Climatol.*, 56, 2317–2334, https://doi.org/10.1175/JAMC-D-17-0004.1, 2017b.

Guo, B., Zhang, F., Zhao, Z., Guo, J., and Li, W.: Retrieval of cloud macro-physical properties using the FY-4A advanced geostationary radiation imager (AGRI) and the geostationary interferometric infrared sounder (GIIRS), *Geophys. Res. Lett.*, 51, e2024GL109772, https://doi.org/10.1029/2024GL109772, 2024.

Guerrette, J. J., Liu, Z., Snyder, C., Jung, B.-J., Schwartz, C. S., Ban, J., Vahl, S., Wu, Y., Baños, I. H., Yu, Y. G., Ha, S., Trémolet, Y., Auligné, T., Gas, C., Ménétrier, B., Shlyaeva, A., Miesch, M., Herbener, S., Liu, E., Holdaway, D., and Johnson, B. T.: Data assimilation for the Model for Prediction Across Scales–Atmosphere with the Joint Effort for Data Assimilation Integration (JEDI–MPAS 2.0.0-beta): Ensemble of En-3DEnVar assimilations, *Geosci. Model Dev.*, 16, 7123–7142, https://doi.org/10.5194/gmd-16-7123-2023, 2023.

Hartmann, B., Gasparini, B., Berry, S. E., and Blossey, P. N.: The life cycle and net radiative effect of tropical anvil clouds, *J. Adv. Model. Earth Syst.*, 10, 3012–3029, https://doi.org/10.1029/2018MS001484, 2018.

Hashino, T., Satoh, M., Hagihara, Y., Kubota, T., Matsui, T., Nasuno, T., and Okamoto, H.: Evaluating cloud microphysics from NICAM against CloudSat and CALIPSO, *J. Geophys. Res. Atmos.*, 118, 7273–7292, https://doi.org/10.1002/jgrd.50564, 2013.

Haynes, J. M., Noh, Y., Miller, S. D., Haynes, K. D., Ebert-Uphoff, I., and Heidinger, A.: Low cloud detection in multilayer scenes using satellite imagery with machine learning methods, *J. Atmos. Oceanic Technol.*, 39, 319–334, https://doi.org/10.1175/JTECH-D-21-0084.1, 2022.

Heidinger, A., Li, Y., and Wanzong, S.: NOAA AWG cloud height algorithm (ACHA), version 3.4, Algorithm Theoretical Basis Document, *NOAA NESDIS Center for Satellite Applications and Research*, 89 pp., https://www.star.nesdis.noaa.gov/jpss/documents/ATBD/ATBD_EPS_Cloud_ACHA_v3.4.pdf, 2018.

Heidinger, A., and Straka, W.: NOAA Enterprise Cloud Mask (ECM), version 1.2, Algorithm Theoretical Basis Document, *NOAA NESDIS Center for Satellite Applications and Research*, 77 pp.,https://www.star.nesdis.noaa.gov/goesr/documents/ATBDs/Enterprise/ATBD_Enterprise_Cloud_Mask_v1.2_2020_10_01.pdf, 2020.

Heidinger, A. K.: ABI cloud height, Algorithm Theoretical Basis Document, *NOAA NESDIS Center for Satellite Applications and Research*, 77 pp., https://www.star.nesdis.noaa.gov/goesr/documents/ATBDs/Baseline/ATBD_GOES-R_Cloud_Height_v3.0_Jul2012.pdf, 2012.

Hong, S., Dudhia, J., and Chen, S.: A revised approach to ice microphysical processes for the bulk parameterization of clouds and precipitation, *Mon. Weather Rev.*, 132, 103–120, https://doi.org/10.1175/1520-0493(2004)132<0103:ARATIM>2.0.CO;2, 2004.

Hong, S.-Y., and Lim, J.-O. J.: The WRF single-moment 6-class microphysics scheme (WSM6), *J. Korean Meteor. Soc.*, 42, 129–151, https://www2.mmm.ucar.edu/wrf/users/workshops/WS2006/abstracts/PSession05/P5_4_Hong.pdf, 2006.

Huang, Y., Siems, S., Manton, M., Protat, A., Majewski, L., and Nguyen, H.: Evaluating Himawari-8 cloud products using shipborne and CALIPSO observations: Cloud-top height and cloud-top temperature, *J. Atmos. Oceanic Technol.*, 36, 2327–2347, https://doi.org/10.1175/JTECH-D-18-0231.1, 2019.

Huang, Y., Wang, Y., Xue, L., and Li, H.: Comparison of three microphysics parameterization schemes in the WRF model for an extreme rainfall event in the coastal metropolitan city of Guangzhou, *China, Atmos. Res.*, 246, 105105, https://doi.org/10.1016/j.atmosres.2020.104939, 2020.

Huang, Y., Liu, Y., Liu, Y., and Knievel, J. C.: Mechanisms for a record-breaking rainfall in the coastal metropolitan city of Guangzhou, China: Observation analysis and nested very large eddy simulation with the WRF model, *J. Geophys. Res. Atmos.*, 124, 1370–1391, https://doi.org/10.1029/2018JD029668, 2019a.

Huang, Y., Liu, Y., Liu, Y., and Knievel, J. C.: Budget analyses of a record-breaking rainfall event in the coastal metropolitan city of Guangzhou, China, *J. Geophys. Res. Atmos.*, https://doi.org/10.1029/2018JD030229, 2019b.

Huo, J., Bi, Y., Wang, H., Zhang, Z., Song, Q., Duan, M., and Han, C.: A comparative study of cloud microphysics schemes in simulating a quasi-linear convective thunderstorm case, *Remote Sens.*, 16, 3259, https://doi.org/10.3390/rs16173259, 2024.

Igel, A. L., van den Heever, S. C., and Johnson, J. S.: Make it a double? Sobering results from simulations using single-moment microphysics schemes, *J. Atmos. Sci.*, 72, 910–925, https://doi.org/10.1175/JAS-D-14-0107.1, 2015.

Illingworth, A. J., Barker, H. W., Beljaars, A., Ceccaldi, M., Chepfer, H., Clerbaux, N., Cole, J., Delanoë, J., Domenech, C., Donovan, D. P., Fukuda, S., Hirakata, M., Hogan, R. J., Huenerbein, A., Kollias, P., Kubota, T., Nakajima, T., Nakajima, T. Y., Nishizawa, T., Ohno, Y., Okamoto, H., Oki, R., Sato, K., Satoh, M., Shephard, M. W., Velázquez-Blázquez, A., Wandinger, U., Wehr, T., and van Zadelhoff, G.-J.: The EarthCARE satellite: the next step forward in global measurements of clouds, aerosols, precipitation, and radiation, *B. Am. Meteorol. Soc.*, 96, 1311-1332, https://doi.org/10.1175/BAMS-D-12-00227.1, 2015.

Imai, T., and Yoshida, R.: Algorithm theoretical basis for Himawari-8 cloud mask product, Meteorological Satellite Center Technical Note No. 61, *Japan Meteorological Agency*, 17 pp., https://www.data.jma.go.jp/mscweb/technotes/msctechrep61-1.pdf, 2016.

Iwabuchi, H., Saito, M., Tokoro, Y., and Coauthors: Retrieval of radiative and microphysical properties of clouds from multispectral infrared measurements, *Prog. in Earth and Planet. Sci*., 3, 32, https://doi.org/10.1186/s40645-016-0108-3, 2016.

Jankov, I., Grasso, L. D., Sengupta, M., Neiman, P. J., Zupanski, D., Zupanski, M., Lindsey, D., Hillger, D. W., Birkenheuer, D. L., Brummer, R., and Yuan, H.: An evaluation of five ARW-WRF microphysics schemes using synthetic GOES imagery for an atmospheric river event affecting the California coast, *J. Hydrometeorol.*, 12, 618–633, doi:10.1175/2010JHM1282.1, 2011.

Jin, D., Oreopoulos, L., Lee, D., Cho, N., and Tan, J.: Contrasting the co-variability of daytime cloud and precipitation over tropical land and ocean, *Atmos. Chem. Phys.*, 18, 3065–3082, https://doi.org/10.5194/acp-18-3065-2018, 2018.

Johnson, B. T., Dang, C., Stegmann, P., Liu, Q., Moradi, I., and Auligné, T.: The Community Radiative Transfer Model (CRTM): Community-focused collaborative model development accelerating research to operations, *Bull. Amer. Meteor. Soc.*, 104, E1817–E1830, https://doi.org/10.1175/BAMS-D-22-0015.1, 2023.

Johnson, B. T., Hocking, J., and Rundle, D.: Comparison of RTTOV and CRTM in JEDI, Visiting Scientist Report NWPSAF-MO_VS-060, version 1.0, *EUMETSAT NWP SAF / JCSDA / Met Office*, 14 pp., https://nwp-saf.eumetsat.int/publications/vs_reports/nwpsaf-mo-vs-060.pdf, 2023.

Johnson, B. T., Dang, C., Rosinski, J., YingtaoMa, StegmannJCSDA and Kasprzyk, P.:JCSDA/crtm: v2.4.1-jedi public release for UFO/JEDI (v2.4.1-jedi), Zenodo [code], https://doi.org/10.5281/zenodo.7823722, 2023.

Joint Center for Satellite Data Assimilation and National Center for Atmospheric Research: JEDI-MPAS Data Assimilation System v3.0.3 (3.0.3), Zenodo [code], https://doi.org/10.5281/zenodo.19209009, 2025.

Jones, T. A., Otkin, J. A., Stensrud, D. J., and Knopfmeier, K.: Assimilation of satellite infrared radiances and Doppler radar observations during a cool season observing system simulation experiment, *Mon. Weather Rev.*, 141, 3273–3299, https://doi.org/10.1175/MWR-D-12-00267.1, 2013.

Jones, T. A., Skinner, P., Knopfmeier, K., Mansell, E., Minnis, P., Palikonda, R., and Smith, W.: Comparison of cloud microphysics schemes in a Warn-on-Forecast system using synthetic satellite objects, *Wea. Forecasting*, 33, 1681–1708, https://doi.org/10.1175/WAF-D-18-0112.1, 2018.

Kanase, R. D., and Salvekar, P. S.: Impact of physical parameterization schemes on track and intensity of severe cyclonic storms in the Bay of Bengal, *Meteorol. Atmos. Phys.*, 127, 537–559, https://doi.org/10.1007/s00703-015-0381-5, 2015.

Khain, A. P., Beheng, K. D., Heymsfield, A., Korolev, A., Krichak, S. O., Levin, Z., Pinsky, M., Phillips, V., Prabhakaran, T., Teller, A., and Coauthors: Representation of microphysical processes in cloud-resolving models: Spectral (bin) microphysics versus bulk parameterization, *Rev. Geophys.*, 53, 247–322, https://doi.org/10.1002/2014RG000468, 2015.

Kim, Y.-S., Wang, X., and Johnson, A.: Impact of microphysics parameterization schemes on the assimilation of GOES-16 ABI all-sky infrared radiances for a bow echo analysis and prediction, *J. Geophys. Res. Atmos.*, 129, e2023JD040046, https://doi.org/10.1029/2023JD040046, 2024.

Köcher, G., Zinner, T., and Knote, C.: Influence of cloud microphysics schemes on weather model predictions of heavy precipitation, *Atmos. Chem. Phys.*, 23, 6255–6269, https://doi.org/10.5194/acp-23-6255-2023, 2023.

Lee, J. C. K., Zhang, H., Barker, D. M., Chen, S., Kumar, R., An, B. W., Sharma, K., and Stephens-Chandramouli, K.: Weather prediction for Singapore—Progress, challenges, and opportunities, *Meteorology*, 1, 394–401, https://doi.org/10.3390/meteorology1040025, 2022.

Letu, H., Nakajima, T. Y., Ishimoto, H., Nagao, T. M., Riedi, J., Baran, A. J., Shang, H., and Kikuchi, M.: Ice cloud properties from Himawari-8/AHI next-generation geostationary satellite: Capability of the AHI to monitor the DC cloud generation process, *IEEE Trans. Geosci. Remote Sens.*, 57, 3229–3239, https://doi.org/10.1109/TGRS.2018.2882803, 2019.

Li, J., Ding, C., Li, F., and Chen, Y.: Effects of single- and double-moment microphysics schemes on the intensity of super typhoon Sarika (2016), *Atmos. Res.*, 238, 104894, https://doi.org/10.1016/j.atmosres.2020.104894, 2020.

Li, J., Geer, A. J., Okamoto, K., Otkin, J. A., Liu, Z., Han, W., and Wang, P.: Satellite all-sky infrared radiance assimilation: Recent progress and future perspectives, *Adv. Atmos. Sci.*, 39, 9–21, https://doi.org/10.1007/s00376-021-1088-9, 2022.

Line, W. E., Schmit, T. J., Lindsey, D. T., and Goodman, S. J.: Use of geostationary super rapid scan satellite imagery by the Storm Prediction Center, *Wea. Forecasting*, 31, 483–494, https://doi.org/10.1175/WAF-D-15-0135.1, 2016.

Lindsey, D., Bikos, D., and Grasso, L.: Using the GOES-16 split window difference to detect a boundary prior to cloud formation, *Bull. Amer. Meteor. Soc.*, 99, 1541–1544, https://doi.org/10.1175/BAMS-D-17-0141.1, 2018.

Lindsey, D., Schmit, T., MacKenzie, W., Jewett, C., Gunshor, M., and Grasso, L.: 10.35 μm: An atmospheric window on the GOES-R Advanced Baseline Imager with less moisture attenuation, *J. Appl. Remote Sens.*, 6, 063598, https://doi.org/10.1117/1.JRS.6.063598, 2012.

Liu, C.-Y., Chiu, C.-H., Lin, P.-H., and Min, M.: Comparison of cloud-top property retrievals from Advanced Himawari Imager, MODIS, CloudSat/CPR, CALIPSO/CALIOP, and radiosonde, *J. Geophys. Res. Atmos.*, 125, e2020JD032683, https://doi.org/10.1029/2020JD032683, 2020.

Liu, X., Griffin, A., Komurcu, M., and Huber, M.: Importance of longwave radiative forcing by icy clouds in maintaining Miocene high-latitude warmth, *Geophys. Res. Lett.*, 52, e2024GL111831, https://doi.org/10.1029/2024GL111831, 2025.

Liu, Z., Snyder, C., Guerrette, J. J., Jung, B.-J., Ban, J., Vahl, S., Wu, Y., Trémolet, Y., Auligné, T., Ménétrier, B., Shlyaeva, A., Herbener, S., Liu, E., Holdaway, D., and Johnson, B. T.: Data assimilation for the Model for Prediction Across Scales–

Atmosphere with the Joint Effort for Data Assimilation Integration (JEDI–MPAS 1.0.0): EnVar implementation and evaluation, *Geosci. Model Dev.*, 15, 7859–7878, https://doi.org/10.5194/gmd-15-7859-2022, 2022.

Liu, Q., and Weng, F.: Advanced doubling-adding method for radiative transfer in planetary atmospheres, *J. Atmos. Sci.*, 63, 3459–3465, https://doi.org/10.1175/JAS3808.1, 2006.

Luo, Y., Zhang, M., Cao, Q., and Wang, L.: An evaluation of the WRF physical parameterizations for extreme rainfall simulation in the Yangtze River Middle Reaches Urban Agglomeration, *Urban Climate*, 58, 102149, https://doi.org/10.1016/j.uclim.2024.102149, 2024.

Mansell, E. R., Ziegler, C. L., and Bruning, E. C.: Simulated electrification of a small thunderstorm with two-moment bulk microphysics, *J. Atmos. Sci.*, 67, 171–194, https://doi.org/10.1175/2009JAS2965.1, 2010.

Marchand, R., Ackerman, T., Smyth, M., and Rossow, W. B.: A review of cloud top height and optical depth histograms from MISR, ISCCP, and MODIS, *J. Geophys. Res. Atmos.*, 115, D16206, https://doi.org/10.1029/2009JD013422, 2010.

Marquis, J. W., Dolinar, E. K., Garnier, A., Campbell, J. R., Ruston, B. C., Yang, P., and Zhang, J.: Estimating the impact of assimilating cirrus cloud-contaminated hyperspectral infrared radiances for numerical weather prediction, *J. Atmos. Ocean. Tech.*, 40, 327–340, https://doi.org/10.1175/JTECH-D-21-0165.1, 2023.

Matsui, T., and Coauthors: Introducing multisensor satellite radiance-based evaluation for regional Earth system modeling, *J. Geophys. Res. Atmos.*, 119, 8450–8475, https://doi.org/10.1002/2013JD021424, 2014.

Mayer, J., Mayer, B., Bugliaro, L., Meerkötter, R., and Voigt, C.: How well can brightness temperature differences of spaceborne imagers help to detect cloud phase? A sensitivity analysis regarding cloud phase and related cloud properties, *Atmos. Meas. Tech.*, 17, 5161–5185, https://doi.org/10.5194/amt-17-5161-2024, 2024.

Medeiros, B., Clement, A. C., Benedict, J. J., and Coauthors: Investigating the impact of cloud-radiative feedbacks on tropical precipitation extremes, *npj Clim. Atmos. Sci.*, 4, 18, https://doi.org/10.1038/s41612-021-00174-x, 2021.

Menzel, W. P., Frey, R. A., Baum, B. A., and Zhang, H.: MODIS cloud top properties and cloud phase algorithm theoretical basis document (Collection 6), NASA MODIS Algorithm Theoretical Basis Document, https://atmosphere-imager.gsfc.nasa.gov/sites/default/files/ModAtmo/MOD06-ATBD_2015_05_01_1.pdf, 2015.

Meyers, M. P., DeMott, P. J., and Cotton, W. R.: New primary ice-nucleation parameterizations in an explicit cloud model, *J. Appl. Meteor. Climatol.*, 31, 708–721, https://doi.org/10.1175/1520-0450(1992)031<0708:NPINPI>2.0.CO;2, 1992.

Milbrandt, J. A., and McTaggart-Cowan, R.: Sedimentation-induced errors in bulk microphysics schemes, *J. Atmos. Sci.*, 67, 3931–3948, https://doi.org/10.1175/2010JAS3541.1, 2010.

Min, M., Li, J., Wang, F., Liu, Z., and Menzel, W. P.: Retrieval of cloud top properties from advanced geostationary satellite imager measurements based on machine learning algorithms, *Remote Sensing of Environment*, 239, 111616, https://doi.org/10.1016/j.rse.2019.111616, 2020.

Mohan, P. R., Srinivas, C. V., Yesubabu, V., and Coauthors: Evaluation of WRF cloud microphysics schemes in explicit simulations of tropical cyclone 'Fani' using wind profiler radar and multi-satellite data products, *Pure Appl. Geophys.*, 181, 2317–2341, https://doi.org/10.1007/s00024-024-03517-w, 2024.

914 Morrison, H., Milbrandt, J. A., Bryan, G. H., Ikeda, K., Tessendorf, S. A., and Thompson, G.: Parameterization of cloud
915 microphysics based on the prediction of bulk ice particle properties. Part II: Case study comparisons with observations
916 and other schemes, *J. Atmos. Sci.*, 72, 312–339, https://doi.org/10.1175/JAS-D-14-0066.1, 2015.
917 Morrison, H., van Lier-Walqui, M., Fridlind, A. M., Grabowski, W. W., Harrington, J. Y., Hoose, C., and Xue, L.: Confronting
918 the challenge of modeling cloud and precipitation microphysics, *J. Adv. Model. Earth Syst.*, 12, e2020MS002170,
919 https://doi.org/10.1029/2019MS001689, 2020.
920 Nam, J., Cho, Y., Lim, K.-S., and Coauthors: Evaluation of four cloud microphysical schemes simulating Arctic low-level
921 clouds observed during the ACLOUD experiment, *Asia-Pac. J. Atmos. Sci.*, 60, 727–740, https://doi.org/10.1007/s13143-
922 024-00378-0, 2024.
923 Nasiri, S. L., and Kahn, B. H.: Limitations of bispectral infrared cloud phase determination and potential for improvement, *J.*
924 *Appl. Meteor. Climatol.*, 47, 2895–2910, https://doi.org/10.1175/2008JAMC1879.1, 2008.
925 Neale, R., and Slingo, J.: The Maritime Continent and its role in the global climate: A GCM study, *J. Climate*, 16, 834–848,
926 https://doi.org/10.1175/1520-0442(2003)016<0834:TMCAIR>2.0.CO;2, 2003.
927 Okamoto, K.: Evaluation of IR radiance simulation for all-sky assimilation of Himawari-8/AHI in a mesoscale NWP system,
928 *Q. J. Roy. Meteor. Soc.*, 143, 1517–1527, https://doi.org/10.1002/qj.3022, 2017.
929 Okugawa, R., Yasunaga, K., Hamada, A., and Yokoi, S.: Numerical study on the precipitation concentration over the western
930 coast of Sumatra Island, *Mon. Weather Rev.*, 152, 689–704, https://doi.org/10.1175/MWR-D-23-0037.1, 2024.
931 Otkin, J. A., and Greenwald, T. J.: Comparison of WRF model simulated and MODIS-derived cloud data, *Mon. Weather Rev.*,
932 136, 1957–1970, https://doi.org/10.1175/2007MWR2293.1, 2008.
933 Otkin, J. A., Greenwald, T. J., Sieglaff, J., and Huang, H.-L.: Validation of a large-scale simulated brightness temperature
934 dataset using SEVIRI satellite observations, *J. Appl. Meteor. Climatol.*, 48, 1613–1626,
935 https://doi.org/10.1175/2009JAMC2142.1, 2009.
936 Otkin, J. A., Lewis, W. E., Lenzen, A. J., McNoldy, B. D., and Majumdar, S. J.: Assessing the accuracy of the cloud and water
937 vapor fields in the Hurricane WRF (HWRF) model using satellite infrared brightness temperatures, *Mon. Weather Rev.*,
938 145, 2027–2046, https://doi.org/10.1175/MWR-D-16-0354.1, 2017.
939 Painemal, D., Minnis, P., and O'Neill, L.: The diurnal cycle of cloud-top height and cloud cover over the southeastern Pacific
940 as observed by GOES-10, *J. Atmos. Sci.*, 70, 2393–2408, https://doi.org/10.1175/JAS-D-12-0325.1, 2013.
941 Panegrossi, G., and Coauthors: Use of the GPM constellation for monitoring heavy precipitation events over the Mediterranean
942 region, *IEEE Journal of Selected Topics in Applied Earth Observations and Remote Sensing*, 9, 2733–2753,
943 https://doi.org/10.1109/JSTARS.2016.2520660, 2016.
944 Park, S., Lee, D.-K., and Lee, J.: Impact of microphysics schemes on the simulation of a tropical cyclone observed during
945 TCS-08, *J. Geophys. Res. Atmos.*, 124, 7421–7442, https://doi.org/10.1029/2019JD032288, 2019.
946 Pavolonis, M., and Calvert, C.: NOAA Enterprise cloud type and cloud phase, version 3, Algorithm Theoretical Basis
947 Document, *NOAA NESDIS Center for Satellite Applications and Research*, 106 pp.,

https://www.star.nesdis.noaa.gov/goesr/documents/ATBDs/Enterprise/ATBD_Enterprise_Cloud_Type_v3_2020-06-01.pdf, 2020.

Pavolonis, M. J., Heidinger, A. K., and Uttal, T.: GOES-R Advanced Baseline Imager (ABI) algorithm theoretical basis document for cloud type and cloud phase, version 2.0, *NOAA NESDIS Center for Satellite Applications and Research*, 86 pp., https://www.star.nesdis.noaa.gov/goesr/docs/ATBD/Cloud_Phase.pdf, 2010.

Pepin, N. C., Arnone, E., Gobiet, A., Haslinger, K., Kotlarski, S., Notarnicola, C., et al.: Climate changes and their elevational patterns in the mountains of the world, *Rev. Geophys.*, 60, e2020RG000730, https://doi.org/10.1029/2020RG000730, 2022.

Rendon, J., and Zhang, Y.: Impact of microphysical parameterizations on satellite all-sky infrared data assimilation and practical predictability of Hurricane Harvey (2017), *J. Geophys. Res. Atmos.*, 130, e2024JD042697, https://doi.org/10.1029/2024JD042697, 2025.

Schmit, T. J., Griffith, P., Gunshor, M. M., Daniels, J. M., Goodman, S. J., and Lebair, W. J.: A closer look at the ABI on the GOES-R series, *Bull. Amer. Meteor. Soc.*, 98, 681–698, https://doi.org/10.1175/BAMS-D-15-00230.1, 2017.

Serra, Y. L., Rutledge, S. A., Chudler, K., and Zhang, C.: Rainfall and convection in ERA5 and MERRA-2 over the northern equatorial western Pacific during PISTON, *J. Climate*, 36, 845–863, https://doi.org/10.1175/JCLI-D-22-0203.1, 2023.

Sieron, S. B., Clothiaux, E. E., Zhang, F., Lu, Y., and Otkin, J. A.: Comparison of using distribution-specific versus effective radius methods for hydrometeor single-scattering properties for all-sky microwave satellite radiance simulations with different microphysics parameterization schemes, *J. Geophys. Res. Atmos.*, 122, 7027–7046, https://doi.org/10.1002/2017JD026494, 2017.

Simón-Moral, A., Dipankar, A., Doan, Q.-V., Sanchez, C., Roth, M., Becker, E., and Coauthors: Urban intensification of convective rainfall over the Singapore–Johor Bahru region, *Q. J. R. Meteorol. Soc.*, 147, 3665–3680, https://doi.org/10.1002/qj.4147, 2021.

Skamarock, W. C., Klemp, J. B., Duda, M. G., Fowler, L. D., Park, S.-H., and Ringler, T. D.: A multiscale nonhydrostatic atmospheric model using centroidal Voronoi tessellations and C-grid staggering, *Mon. Weather Rev.*, 140, 3090–3105, https://doi.org/10.1175/MWR-D-11-00215.1, 2012.

Skamarock, W. C., Duda, M. G., Ha, S., and Park, S.-H.: Limited-area atmospheric modeling using an unstructured mesh, *Mon. Weather Rev.*, 146, 3445–3460, https://doi.org/10.1175/MWR-D-18-0155.1, 2018.

Sokol, A. B., and Hartmann, D. L.: Tropical anvil clouds: Radiative driving toward a preferred state, *J. Geophys. Res. Atmos.*, 125, e2020JD033107, https://doi.org/10.1029/2020JD033107, 2020.

Spang, R., Müller, R., and Rap, A.: Radiative effect of thin cirrus clouds in the extratropical lowermost stratosphere and tropopause region, *Atmos. Chem. Phys.*, 24, 1213–1230, https://doi.org/10.5194/acp-24-1213-2024, 2024.

Stephens, G. L., Shiro, K. A., Hakuba, M. Z., and Coauthors: Tropical deep convection, cloud feedbacks and climate sensitivity, *Surv. Geophys.*, 45, 1903–1931, https://doi.org/10.1007/s10712-024-09831-1, 2024.

Sunny Lim, K., Chang, E., Sun, R., Kim, K., Tapiador, F. J., and Lee, G.: Evaluation of simulated winter precipitation using WRF-ARW during the ICE-POP 2018 field campaign, *Wea. Forecasting*, 35, 2199–2213, https://doi.org/10.1175/WAF-D-19-0236.1, 2020.

Susskind, J., Blaisdell, J. M., Iredell, L., and Keita, F.: Improved temperature sounding and quality control methodology using AIRS/AMSU data: The AIRS Science Team Version 5 retrieval algorithm, *IEEE Trans. Geosci. Remote Sens.*, 49, 883–907, https://doi.org/10.1109/TGRS.2010.2070508, 2011.

Tao, W.-K., Iguchi, T., Lang, S., Li, X., Mohr, K., Matsui, T., van den Heever, S. C., and Braun, S.: Relating vertical velocity and cloud/precipitation properties: A numerical cloud ensemble modeling study of tropical convection, *J. Adv. Model. Earth Syst.*, 14, e2021MS002677, https://doi.org/10.1029/2021MS002677, 2022.

Thompson, M., Tewari, K., Ikeda, K., Tessendorf, S., Weeks, C., Otkin, J. A., and Kong, F.: Explicitly coupled cloud physics and radiation parameterizations and subsequent evaluation in WRF high-resolution convective forecasts, *Atmos. Res.*, 168, 92–104, https://doi.org/10.1016/j.atmosres.2015.09.005, 2016.

Tong, M., and Xue, M.: Simultaneous estimation of microphysical parameters and atmospheric state with radar data and ensemble square-root Kalman filter. Part I: Sensitivity analysis and parameter identifiability, *Mon. Weather Rev.*, 136, 1630–1648, https://doi.org/10.1175/2007MWR2070.1, 2008.

Trémolet, Y., and Auligné, T.: The Joint Effort for Data Assimilation Integration (JEDI), *JCSDA Quarterly Newsletter*, 66, 1–5, https://doi.org/10.25923/RB19-0Q26, 2020.

Van Weverberg, K., and Coauthors: Comparison of one-moment and two-moment bulk microphysics for high-resolution climate simulations of intense precipitation, *Atmos. Res.*, 147, 145–161, https://doi.org/10.1016/j.atmosres.2014.05.012, 2014.

Van Weverberg, K., Vogelmann, A. M., Lin, W., and Coauthors: The role of cloud microphysics parameterization in the simulation of mesoscale convective system clouds and precipitation in the tropical western Pacific, *J. Atmos. Sci.*, 70, 1104–1128, https://doi.org/10.1175/JAS-D-12-0104.1, 2013.

Waliser, D. E., Li, J. L. F., Woods, C. P., and Coauthors: Cloud ice: A climate model challenge with signs and expectations of progress, *J. Geophys. Res. Atmos.*, 114, D08209, https://doi.org/10.1029/2008JD010015, 2009.

Wall, C. J., Hartmann, D. L., Thieman, M. M., Smith, W. L., and Minnis, P.: The life cycle of anvil clouds and the top-of-atmosphere radiation balance over the tropical west Pacific, *J. Climate*, 31, 10059–10080, https://doi.org/10.1175/JCLI-D-18-0154.1, 2018.

Wang, C., Yang, P., Platnick, S., Heidinger, A. K., Baum, B. A., Greenwald, T., Zhang, Z., and Holz, R. E.: Retrieval of ice cloud properties from AIRS and MODIS observations based on a fast high-spectral-resolution radiative transfer model, *J. Appl. Meteor. Climatol.*, 52, 710–726, https://doi.org/10.1175/JAMC-D-12-020.1, 2013.

Wang, X., Chipilski, H. G., Bishop, C. H., Satterfield, E., Baker, N., and Whittaker, J.: A multiscale local gain form ensemble transform Kalman filter (MLGETKF), *Mon. Weather Rev.*, 149, 605–622, https://doi.org/10.1175/MWR-D-20-0290.1, 2021.

Wang, Y., Su, H., Jiang, J. H., Xu, F., and Yung, Y. L.: Impact of cloud ice particle size uncertainty in a climate model and implications for future satellite missions, *J. Geophys. Res. Atmos.*, 125, e2019JD032119, https://doi.org/10.1029/2019JD032119, 2020.

Wang, Y., and Zhao, C.: Can MODIS cloud fraction fully represent the diurnal and seasonal variations at DOE ARM SGP and Manus sites? *J. Geophys. Res. Atmos.*, 122, 329–343, https://doi.org/10.1002/2016JD025954, 2017.

Wang, Y., Liu, Z., Yang, S., Min, J., Chen, L., Chen, Y., and Zhang, T.: Added value of assimilating Himawari-8 AHI water vapor radiances on analyses and forecasts for the "7.19" severe storm over North China, *J. Geophys. Res. Atmos.*, 123, 3374–3394, https://doi.org/10.1002/2017JD027697, 2018.

Wang, T., Zhu, J., Lei, H., Shi, Y., Guo, J., and Gao, Z.: Comparison of microphysics parameterization schemes on cloud macrophysics forecasts for mixed convective–stratiform cloud events, *Atmos. Res.*, 277, 106284, https://doi.org/10.1016/j.atmosres.2022.106284, 2022.

Wang, T., Zhu, J., Lei, H., Shi, Y., Guo, J., and Gao, Z.: Comparison of microphysics parameterization schemes on cloud macrophysics forecasts for mixed convective-stratiform cloud events, *Atmos. Res.*, 277, 106284, https://doi.org/10.1016/j.atmosres.2022.106284, 2022.

Wehr, T., Kubota, T., Tzeremes, G., Wallace, K., Nakatsuka, H., Ohno, Y., Koopman, R., Rusli, S., Kikuchi, M., Eisinger, M., Tanaka, T., Taga, M., Deghaye, P., Tomita, E., and Bernaerts, D.: The EarthCARE mission – science and system overview, *Atmos. Meas. Tech.*, 16, 3581–3608, https://doi.org/10.5194/amt-16-3581-2023, 2023.

Wheatley, D. M., Yussouf, N., and Stensrud, D. J.: Ensemble Kalman filter analyses and forecasts of a severe mesoscale convective system using different choices of microphysics schemes, *Mon. Weather Rev.*, 142, 3243–3263, https://doi.org/10.1175/MWR-D-13-00260.1, 2014.

Xu, K.-M., and Randall, D. A.: A semiempirical cloudiness parameterization for use in climate models, *J. Atmos. Sci.*, 53, 3084–3102, https://doi.org/10.1175/1520-0469(1996)053<3084:ASCPFU>2.0.CO;2, 1996.

Yao, B., Liu, C., Yin, Y., Zhang, P., Min, M., and Han, W.: Radiance-based evaluation of WRF cloud properties over East Asia: Direct comparison with FY-2E observations, *J. Geophys. Res. Atmos.*, 123, 4613–4629, https://doi.org/10.1029/2017JD027600, 2018.

Yang, K., et al.: On downward shortwave and longwave radiations over high-altitude regions: observations and modeling in the Tibetan Plateau, *Atmos. Res.*, 150, 38–51, https://doi.org/10.1016/j.atmosres.2014.01.016, 2010.

Yokoi, S., Mori, S., Katsumata, M., Geng, B., Yasunaga, K., Syamsudin, F., Nurhayati, N., and Yoneyama, K.: Diurnal cycle of precipitation observed in the western coastal area of Sumatra Island: Offshore preconditioning by gravity waves, *Mon. Weather Rev.*, 145, 3745–3761, https://doi.org/10.1175/MWR-D-16-0468.1, 2017.

Zhang, X., Jiang, L., Liu, Z., Sun, T., Wang, W., and Chen, I.-H.: Assessing Cloud Representation in Two Microphysics Schemes of MPAS-Atmosphere Model (version 8.2.2) with Himawari-9 AHI Observations, Zenodo [code], https://doi.org/10.5281/zenodo.19925596, 2026a.

Zhang, X., Liu, Z., Sun, T., and Chen, I.-H.: Processed Observation Datasets for "Assessing Cloud Representation in Two Microphysics Schemes of the MPAS-Atmosphere Model (Version 8.2.2) Using Himawari-9 AHI Observations", Zenodo [data set], https://doi.org/10.5281/zenodo.20312122, 2026b.

Zhang, X., Wei, W., Tao, S., Zhiquan, L., and Chen, I.-H.: MPAS-Model v8.2.2 with WSM6 and NSSL Microphysics, Zenodo [code], https://doi.org/10.5281/zenodo.23487937, 2026c.

Zhang, Y., Fan, J., Li, Z., and Rosenfeld, D.: Impacts of cloud microphysics parameterizations on simulated aerosol–cloud interactions for deep convective clouds over Houston, *Atmos. Chem. Phys.*, 21, 2363–2381, https://doi.org/10.5194/acp-21-2363-2021, 2021.

Zhang, Y., Wang, Y., Liu, G., and Guo, J.: Satellite-based assessment of various cloud microphysics schemes in simulating typhoon hydrometeors, *Adv. Meteorol.*, 2019, 3168478, https://doi.org/10.1155/2019/3168478, 2019.

Zhu, K., Xue, M., Yang, N., and Zhang, C.: How well does 4-km WRF model predict three-dimensional reflectivity structure over China as compared to radar observations?, *J. Geophys. Res. Atmos.*, 128, e2022JD038143, doi:10.1029/2022JD038143, 2023.

Zhu, Z., Gu, J., Xu, B., and Shi, C.: Characterization of Himawari-8/AHI to Himawari-9/AHI infrared observations continuity, *Int. J. Remote Sens.*, 45, 121–142, https://doi.org/10.1080/01431161.2023.2293476, 2023.